

Incommensurate magnetic modulation in K-rich cryptomelane, $\text{K}_x\text{Mn}_8\text{O}_{16}$ ($x \approx 1.45$)

Liam A. V. Nagle-Cocco ^{a,†,‡,¶} Joshua D. Bocarsly ^{b,†,‡} Krishnakanth Sada
^{c,§,†} Nicola D. Kelly,[†] Mathias A. Kiefer,[¶] Emmanuelle Suard,^{||} Sarah J. Day,[⊥]
Cheng Liu,[†] Clare P. Grey,[‡] Prabeer Barpanda,[§] Clemens Ritter,^{||} and Siân E.
Dutton ^{d,†}

[†]*Cavendish Laboratory, University of Cambridge, Cambridge, CB3 0HE, United Kingdom.*

[‡]*Yusuf Hamied Department of Chemistry, University of Cambridge, Cambridge, CB2 1EW,
United Kingdom.*

[¶]*Stanford Synchrotron Radiation Lightsource, SLAC National Accelerator Laboratory,
Menlo Park, California 94025, United States.*

[§]*Faraday Materials Laboratory (FaMaL), Materials Research Centre, Indian Institute of
Science, C. V. Raman Avenue, Bangalore, 560012, India.*

^{||}*Institut Laue-Langevin, 71 avenue des Martyrs, CS 20156, cedex 9, Grenoble 38042,
France.*

[⊥]*Diamond Light Source, Ltd., Harwell Science and Innovation Campus, Didcot,
Oxfordshire OX11 0DE, United Kingdom.*

E-mail:

^aEmail: lnc@stanford.edu

^bPresent address: Department of Chemistry, University of Houston, United States of America.

^cPresent address: Xerion Advanced Battery Corporation, Dayton, Ohio, United States of America.

^dEmail: sed33@cam.ac.uk

Abstract

Cryptomelane is a hollandite-like material consisting of K^+ cations in an α - MnO_2 tunnel-like crystallographic motif. A sample with stoichiometry $K_{1.448(3)}Mn_8O_{16}$ has been synthesised and its magnetic properties investigated using variable-temperature magnetic susceptibility, heat capacity, and neutron powder diffraction. Three distinct transitions at $T_1 = 184\text{ K}$, $T_2 = 54.5\text{ K}$, and $T_3 = 24\text{ K}$ are observed. At T_1 there is a subtle tetragonal \rightarrow monoclinic transition associated with Mn^{3+}/Mn^{4+} ordering, and a set of non-magnetic superstructure peaks emerge; these could not be indexed definitively and are indicative of an ordering that is incommensurate with the unit cell. Magnetic Bragg peaks emerge below $T_2 = 54.5\text{ K}$, and their positions indicate an incommensurate modulated magnetic structure. The model consistent with the data is a dual- \vec{k}_{mag} structure with a ferromagnetic $|\vec{k}_{\text{mag}}| = 0$ component and an incommensurate \vec{k}_{mag} parallel to the α - MnO_2 tunnels [$|\vec{k}_{\text{mag}}| = 0.36902(15)$], with the latter most likely to be helical. The period of oscillation of the helical component is in line with predictions based on a Heisenberg spin Hamiltonian [Mandal *et al.* Phys. Rev. B 90, 104420 (2014)]. Below $T_3 = 24\text{ K}$, there is a magnetic transition, which gives rise to a different set of magnetic Bragg peaks indicative of a highly complex magnetic structure.

Introduction

α - MnO_2 is a polymorph of $Mn^{4+}O_2$ comprised of corner-sharing rutile-like ribbons of MnO_6 octahedra which share edges to form a tunnel structure.¹ This structural motif has led to significant interest because in addition to doping within the MnO_2 framework,² it is also possible to incorporate dopants into the tunnels. α - MnO_2 is commonly studied in an X -doped form, X_xMnO_2 with X a large cation like K^+ , Ba^{2+} , or Na^+ .^{1,3,4} In this work we focus on the K -doped variant, $K_xMn_x^{3+}Mn_{8-x}^{4+}O_{16}$, which is a naturally-occurring mineral called cryptomelane, and contains mixed Mn valence. K^+ cations can be incorporated into

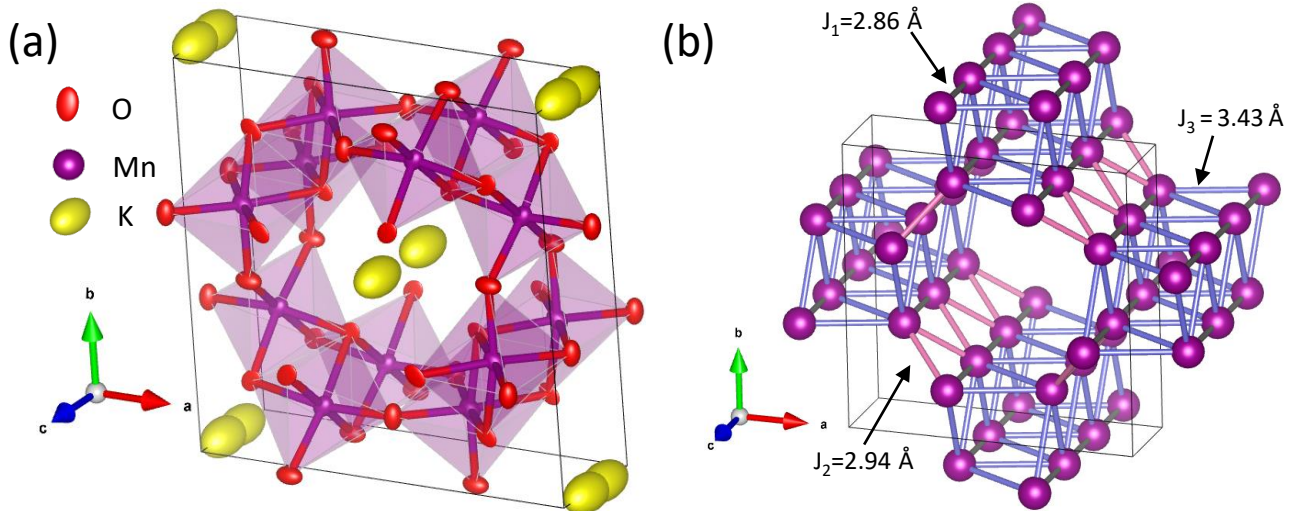


Figure 1: (a) Crystallographic structure of cryptomelane in the $I4/m$ space group, as viewed at a slight angle from the c -axis, with atoms displayed as ellipsoids of 95% probability. Ellipsoids are constructed based on refined anisotropic atomic displacement parameters. Red: O; purple: Mn; yellow: K. (b) The Mn lattice of cryptomelane only, showing the three nearest Mn-Mn interactions. Grey: J_1 , pink: J_2 , purple: J_3 . The exchange interactions follow the notation of Crespo *et al.*¹³

the tunnel structure to a maximum of $x = 2$, as shown in Figure 1(a), with the doping limited by the occupancy of K in the tunnels. Due to the large tunnels ($\sim 6 \text{ \AA}$ in diameter), cryptomelane has significant potential for various applications. For example, it can serve as the positive electrode in K-ion^{5,6} and Zn-ion⁷ batteries, for water splitting via the oxygen evolution reaction,⁸ and for oxidising organic pollutants such as toluene and ethyl acetate.^{9–12}

Cryptomelane has been studied extensively for its magnetic properties,^{13–23} which stem from its frustration-prone structure. The frustration arises due to competition between the three neighbouring Mn-Mn magnetic interactions. In the notation of Crespo *et al.* (2013),¹³ these are J_1 : interactions between edge-sharing MnO_6 octahedra where the Mn-Mn distance is parallel with the c -axis and the direction of the tunnels; J_2 : a second edge-sharing interaction between MnO_6 octahedra where the Mn-Mn interaction is approximately 29° from the ab -plane; and J_3 : corner-sharing MnO_6 octahedra, which are separated from one another by bond-angle $\theta_{\text{Mn-O-Mn}} \approx 130^\circ$. These are labelled schematically in Figure 1(b).

The magnetic properties of cryptomelane are found to be highly dependent on the K-

stoichiometry, x , with quite different temperature-dependent magnetic behaviour in the range $0.72 < x < 1$ compared with $1 < x < 2$. For the lower x -range, short-range ferromagnetic or ferrimagnetic correlations occur along with formation of a spin glass, with a transition reported in the range $33.1 < T_g(\text{K}) < 50$.^{15,18,19} We are primarily interested in the higher- x compositional range, where there are 3 reported transitions observed in magnetometry, and a lack of consensus on their origin.^{16,17,19,21-23} These three transitions are denoted, in descending order by temperature, as T_1 , T_2 , and T_3 , in this and other works.¹⁷ The majority of studies of the magnetic structure of cryptomelane with $x \geq 1$ report two magnetic transitions, one at $T_2 \approx 55$ K and another in the range $T_3 \approx 20 - 25$ K. In some works, a higher temperature transition observed by magnetisation and electrical transport measurements, occurring in the range $180 < T_1(\text{K}) < 250$, is assigned to charge ordering of Mn^{3+} and Mn^{4+} .^{17,19} No associated superstructure has thus far been reported by diffraction. Based on magnetic susceptibility measurements, the transition at $T_2 \approx 55$ K is described as having non-collinear antiferromagnetic ordering, helical magnetism or weak ferromagnetism.^{17,19,21,22} Studies on single crystals^{16,17} involving isothermal magnetisation measurements show that there is significant anisotropy and irreversibility when the field is applied perpendicular to the tunnels, indicating a net moment in the ab -plane.

Below the lower temperature transition $T_3 \approx 20$ K, some studies report formation of a spin glass-like state.^{22,23} This is based on observed frequency dependence of transition temperature in AC susceptibility and divergence between temperature-dependent susceptibility during cooling in the presence/absence of a magnetic field. Additionally, the spin glass-like state is believed to relate to observed magnetic memory behaviour,^{22,23} in which holding the material at a particular temperature in a magnetic field during cooling leads to features at that temperature during subsequent heating.²³ A prior neutron diffraction study on a sample of $\text{K}_{1.72}\text{Mn}_8\text{O}_{16}$ observed a different set of magnetic Bragg peaks in each temperature regime;²⁴ the authors did not solve the magnetic structure, but do suggest an incommensurate magnetic structure in the higher temperature regime and a commensurate magnetic

structure below ~ 25 K. Besides this, no neutron diffraction experiments have so far explored the long-range magnetic order in cryptomelane of any stoichiometry, although a study on the Ba-analog²⁵ has found modulated magnetism, commensurate with the unit cell.

In this work, we present the first magnetic structure solution from a neutron diffraction study on a sample of cryptomelane with stoichiometry $\text{K}_{1.448(3)}\text{Mn}_8\text{O}_{16}$ and average Mn oxidation state of approximately +3.75. Our results are compared to the theory, developed by Sato *et al.*,^{16,17} in which simultaneous charge- and spin-modulations give rise to a helical ordering with a net moment. We find evidence in favour of this helical ferrimagnetism below 54.5 K. We also observe the existence of a set of magnetic Bragg peaks, below the transition at $T_3 \approx 24$ K, albeit at different positions compared with above T_3 , which had previously been proposed to be a glass transition. This persistence of long-range magnetic order is inconsistent with prior reports of a bulk spin glass-like state. Furthermore, we observe a subtle structural transition at T_1 K, which is associated with the emergence of a set of non-magnetic superstructure peaks which could not be indexed definitively, but are indicative of a structural ordering which is incommensurate with the unit cell.

Methods

Sample preparation. Cryptomelane was prepared, in a quantity of several grams, using a solid-state synthesis route with a target composition of $\text{K}_{1.33}\text{Mn}_8\text{O}_{16}$. The precursors in the molar ratio of 1.33:8 KNO_3 to MnCO_3 (99.994% and 99.9% purity respectively; both from Alfa Aesar) were mixed thoroughly using agate mortar and pestle, with a 5% molar excess of KNO_3 to account for K-loss during high-temperature calcination. Planetary mixing in ethanol was carried out for ~ 15 minutes. The resultant powder was annealed in air at 500°C for ~ 4 hours, with a heating rate of 5°C min^{-1} . Samples were cooled to room temperature by switching off the furnace.

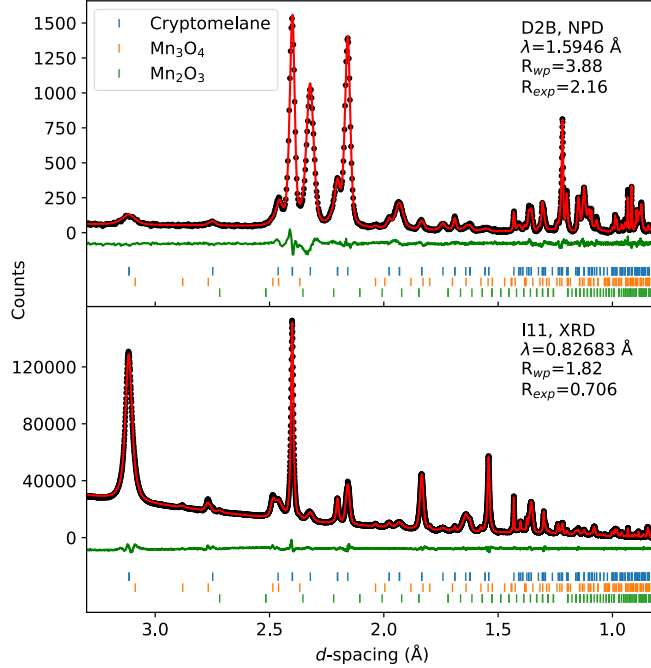


Figure 2: Experimental (black points) and calculated (red line, modelled by combined Rietveld refinement) diffraction data at room temperature for synchrotron XRD (bottom) and neutron diffraction (top). The difference between the model and data is shown in green. Blue tick-marks indicate nuclear Bragg peaks due to cryptomelane $\text{K}_{1.448(3)}\text{Mn}_8\text{O}_{16}$, and orange and green tick-marks indicate nuclear Bragg peaks due to the Mn_3O_4 (2.8(3)wt%) and Mn_2O_3 (0.049(5)wt%) impurities respectively. The R_{wp} and R_{exp} of the fit to each dataset are shown in the figure panels, and the values for the total refinement were 1.87% and 0.750% respectively (to 3 significant figures).

Magnetisation measurements. A Quantum Design Magnetic Properties Measurement System (MPMS-3) was used for DC susceptibility and isothermal magnetisation measurements. Measurements were taken during warming after cooling in zero field (ZFC-W) and in the measuring field (FC-W), where the measuring field was 200 Oe. Isothermal magnetisation measurements were performed in an external magnetic field between ± 70 kOe.

A Quantum Design 9 T Physical Properties Measurement System (PPMS) using the ACMS-II option was used for AC susceptibility. Measurements were taken with an AC driving field of 10 Oe in a static field of 10 Oe at 500 Hz, 1001 Hz, 1501 Hz, 2002 Hz, and 4004 Hz.

Heat capacity. A Quantum Design PPMS was used for heat capacity measurements. As is common for thermally insulating samples²⁶⁻³⁰ the sample was mixed with silver powder (Alfa Aesar, 99.99%, -635 mesh) in a 1:1 mass ratio to increase the conductivity; this was accounted for using tabulated temperature-dependent heat capacity of silver from Ref. 31. Apiezon N grease was used to provide thermal contact between the sample platform and the pellet. The lattice contribution to the heat capacity was estimated and accounted for using a Debye temperature³² $T_D = 470(18)$ K (see Figure S2 of Supplementary Information) fit using SCIPY.³³ Uncertainty in fitted parameters was obtained by weighting datapoints while assuming error is due to the precision of the sample mass, and using the diagonal elements of the covariance matrix resulting from the fit.

Diffraction. Synchrotron X-ray Diffraction (XRD) was performed using the I11 instrument^{34,35} at Diamond Light Source. As the measurements were taken during different runs, $\lambda = 0.82683$ Å for room temperature; $\lambda = 0.825223$ Å for low temperatures from 300 K to 100 K. Synchrotron diffraction at I11 used the Mythen-2 position-sensitive detector, with a collection time of ~ 20 seconds per diffraction pattern. The sample was contained in a 0.5 mm diameter glass capillary, sealed with epoxy (Loctite Double Bubble). For the low-temperature synchrotron X-ray diffraction between 100 K and 300 K, a discrete temperature spacing of 1 K was used. Low-temperature laboratory XRD below 100 K was performed using a Bruker D8 Discover diffractometer (Cu $K\alpha$; $\lambda = 1.541$ Å), with an Oxford Cryosystems PheniX stage to cool using liquid He.

Constant-wavelength neutron diffraction experiments were performed at the Institut Laue-Langevin. Measurements were performed on the high-resolution powder diffractometer D2B (room-temperature; $\lambda = 1.5946$ Å) and the high-intensity powder diffractometer D20 (2.5 K, 40 K, 44 K, 47 K, and 60 K; $\lambda = 2.4108$ Å). Both neutron and X-ray measurements were performed on aliquots of the same sample.

Diffraction analysis. Structural diffraction data were analysed using the software package TOPAS-ACADEMIC³⁶ using Rietveld refinement.³⁷ The room-temperature data were analysed by combined refinement of the room-temperature I11 and D2B data, whereas the variable-temperature synchrotron diffraction data were analysed by sequential Rietveld refinement in which each diffraction pattern is analysed in turn on heating, with the starting parameters of a refinement being the refined parameters from the previous diffraction pattern. The background was fitted by a Chebyshev polynomial (order 15 and 6 for synchrotron data and neutron data respectively in the room-temperature refinement; order 20 in the sequential refinement of synchrotron XRD). A fixed Thompson-Cox-Hastings pseudo-Voigt peak-shape refined from standard Si data was used³⁸ for the instrumental contribution to the synchrotron data, and the sample contribution to the peak-shape was accounted for using Stephens' function for anisotropic microstrain broadening³⁹ convoluted with a Lorentzian particle size broadening function. The neutron peak shape was modelled using the Lorentzian and Gaussian particle size functions, and also Stephens' function.³⁹ Peak asymmetry was accounted for using a simple axial divergence model. All atomic positions, lattice parameters, and atomic displacement parameters were refined within symmetry constraints. Anisotropic atomic displacement parameters (ADPs)⁴⁰ were refined for K and O, whereas isotropic thermal displacement parameters were used for Mn. Mn occupancies were fixed to 100% while all K and O occupancies were initially refined. The O2 site was fully occupied within error, and so was fixed at 100% for the final refinement.

Magnetic diffraction analysis was performed using FULLPROF.⁴¹ Diffraction difference patterns were calculated by subtracting the neutron 60 K dataset from lower-temperature diffraction patterns using LAMP.⁴² Candidate magnetic propagation vectors (\vec{k}_{mag}) were found using K Search, a tool in FULLPROF, using the position of peaks in the difference pattern. Precise values of parameters in \vec{k}_{mag} were refined against the difference pattern by Le Bail refinement.⁴³ BASIREPS^{44,45} was used to calculate the Irreducible Representations (IRs) for a given \vec{k}_{mag} (see Section VII of Supplementary Information) and their basis vectors

(BVs).

In FULLPROF, the March-Dollase model⁴⁶ was used to account for preferred orientation in the sample used for low-temperature neutron diffraction due to slightly non-spherical particle shape (see Figure S1 of Supplementary Information).

Results

Structural characterisation

The room temperature structure of cryptomelane, $K_xMn_8O_{16}$, was investigated by neutron and X-ray diffraction on the D2B instrument at the ILL and the I11 instrument at Diamond Light Source, respectively. Combined Rietveld refinement was carried out with the previously-reported $I4/m$ (space group #87) structure.⁴⁷ In this tetragonal symmetry structure, there is a single Mn site, $8h(x, y, 0)$, and two inequivalent oxygen sites both at $8h(x, y, 0)$. K is located within the tunnels in a partially occupied site, $4e(0, 0, z)$.

Structural parameters and refinement R-factors from a combined Rietveld refinement on the room-temperature X-ray and neutron diffraction data are shown in Table 1, with the refined and calculated profile shown in Figure 2. These measurements indicate the presence of a 2.8(3)% (by weight) Mn_3O_4 impurity phase ($I4_1/amd$ space group, #121). There are also a number of very small peaks, visible only in the synchrotron diffraction data, which are consistent with the presence of trace amounts of Mn_2O_3 ($Ia\bar{3}$; #206); this impurity phase refines to 0.049(5)% (by weight). Such Mn_xO_{x+1} impurities are a common occurrence in magnetic studies of manganese-containing materials.⁴⁸⁻⁵⁰ Refinement of K site occupancy gives $x = 1.448(3)$ in $K_xMn_8O_{16}$, with the excess K, as compared with the target composition of $K_{1.33}Mn_8O_{16}$, likely a consequence of the formation of the K-free Mn_3O_4/Mn_2O_3 impurity phases and the use of excess K during synthesis. The room-temperature Rietveld-refined crystallographic model is consistent with the reported crystal structure for cryptomelane.

In the Rietveld fit, anisotropic strain was implemented using Stephens' function.³⁹ Re-

Table 1: The crystallographic parameters of cryptomelane $K_{1.448(3)}Mn_8O_{16}$ at room temperature, as obtained by a combined Rietveld refinement of XRD data from the I11 instrument and neutron diffraction using the D2B instrument. Mn and O2 occupancies were fixed at 1.

Space group	$I4/m$
$a = b / \text{\AA}$	9.84942(9)
$c / \text{\AA}$	2.862033(17)
$V / \text{\AA}^3$	277.649(6)
χ^2	6.21
R_{wp}	1.87
R_{exp}	0.750
K at $4e (0, 0, z)$	
$z(K)$	0.3559(11)
$U_{11} / \text{\AA}^2$	0.0259(11)
$U_{33} / \text{\AA}^2$	0.093(4)
occupancy(K)	0.3621(8)
Mn at $8h (x, y, 0)$	
$x(Mn)$	0.34939(4)
$y(Mn)$	0.16575(5)
$U_{11}(Mn) / \text{\AA}^2$	0.0086(4)
$U_{22}(Mn) / \text{\AA}^2$	0.0069(4)
$U_{33}(Mn) / \text{\AA}^2$	0.0061(3)
$U_{12}(Mn) / \text{\AA}^2$	0.0027(3)
O at $8h (x, y, 0)$	
$x(O1)$	0.15315(12)
$y(O1)$	0.20283(10)
$U_{11}(O1) / \text{\AA}^2$	0.0103(9)
$U_{22}(O1) / \text{\AA}^2$	0.0158(6)
$U_{33}(O1) / \text{\AA}^2$	0.0028(6)
$U_{12}(O1) / \text{\AA}^2$	0.0000(7)
occupancy(O1)	0.9801(12)
$x(O2)$	0.54063(12)
$y(O2)$	0.16551(13)
$U_{11}(O2) / \text{\AA}^2$	0.0055(8)
$U_{22}(O2) / \text{\AA}^2$	0.0121(8)
$U_{33}(O2) / \text{\AA}^2$	0.0030(6)
$U_{12}(O2) / \text{\AA}^2$	0.0005(7)
Bond lengths	
Mn-Mn (J_1 ; x 2) / \AA	2.862033(17)
Mn-Mn (J_2 ; x 2) / \AA	2.9385(8)
Mn-Mn (J_3 ; x 4) / \AA	3.4321(6)
Mn-O1 (x 1) / \AA	1.967(1)
Mn-O1 (x 2) / \AA	1.9297(7)
Mn-O2 (x 1) / \AA	1.884(1)
Mn-O2 (x 2) / \AA	1.8942(8)
Mn-O-Mn bond angles	
Mn-O1-Mn / $^\circ$	97.89(5)
Mn-O2-Mn / $^\circ$	98.13(6)

fined strain parameters obtained from the synchrotron data, $S_{004} = 2970(60)$ and $S_{400} = 1637(9)$, show the anisotropic nature of this strain. Anisotropic strain likely comes from the tunnel dimensions in hollandites being highly dependent on the occupancy of the large cation in the tunnels, as shown by previous works on cryptomelane⁵ and its silver analog $\text{Ag}_x\text{Mn}_8\text{O}_{16}$ ($1.14 \leq x \leq 1.66$).⁵¹ The strain is likely in part due to local variations in the K content and resultant variations on Mn oxidation state (due to the requirement for local charge balancing) leading to local differences.

Anisotropic ADPs for the K^+ cations refined to be highly anisotropic, with the $U_{33} = 0.093(4) \text{ \AA}^2$ several times larger than $U_{22} = U_{11} = 0.0259(11) \text{ \AA}^2$, as shown in Figure 1(a). This is consistent with previous work⁵² which showed that the anisotropic K^+ ADPs could also be modelled using a split-site approach. The high degree of anisotropy in the K^+ ADPs could be due to static disorder from K^+ ions occupying a range of z positions in the $4e$ $(0, 0, z)$ sites, for instance due to different K^+ positioning in proximity to a K^+ cation or vacancy. Alternatively, there may be dynamic disorder from highly mobile K^+ hopping between adjacent sites.

The ADPs for the two oxygen sites show different behaviour, likely resulting from the different degrees of freedom due to this MnO_6 connectivity. The local environments of the two oxygen sites, O1 and O2, are different. O1 oxygen sites share bonds with K and Mn, and occur as the shared vertices of edge-sharing MnO_6 octahedra, whereas O2 oxygen sites are further from K than O1, and are the shared vertices of three corner-sharing MnO_6 octahedra. Refinement of site occupancies for oxygen indicated oxygen vacancies on one of the two O sites, with a refined occupancy on the O1 site of 0.9801(12). This corresponds to $\text{K}_{1.448(3)}\text{Mn}_8\text{O}_{15.841(9)}$, and from this stoichiometry we calculate an average Mn oxidation of +3.779(2). For simplicity, we will use the nominal oxygen content in all further discussion.

Another way to determine oxidation state is using the empirical bond valence sum (BVS) relation between bond length and oxidation state,⁵³ which was previously applied to $\text{Ba}_{1.2}\text{Mn}_8\text{O}_{16}$.²⁵ For the MnO_6 octahedra in this study, we can obtain Mn valence V using

the following equation:

$$V = \sum_{i=1}^6 \exp \left[\frac{r_0 - r_i}{B} \right] \quad (1)$$

where the empirical parameters $r_0 = 1.762 \text{ \AA}$ and $B = 0.34 \text{ \AA}$ for Mn^{4+} (taken from Ref. 53), and r_i are the Mn-O bond lengths. Using this approach, we obtain an average Mn oxidation state of $+3.826(4)$. This is close, although not within error of the value calculated from stoichiometry. Deviation from BVS behaviour could occur because the average structure is a superposition of multiple differing local structures caused by Mn charge disorder and Jahn–Teller distortions.

The MnO_6 octahedra are all identical in the average $I4/m$ structure. They exhibit four different Mn-O bond lengths between $1.8837(13) \text{ \AA}$ and $1.967(1) \text{ \AA}$. It is possible that some portion of the bond length distortion may be in part the result of averaging multivalent MnO_6 octahedra, some of which contain Jahn–Teller-active Mn^{3+} , but the competing geometric interactions on each octahedron add complexity. These bond length values and multiplicity does not lend itself to simple deconvolution of the Q_2 and Q_3 van Vleck modes with E_g symmetry typical of a Jahn–Teller distortion,^{54,55} unlike for instance the perovskite LaMnO_3 ⁵⁶ which has three unique bond lengths each mutually perpendicular, and so possible signatures of a Jahn–Teller distortion cannot be determined. The bond-length distortion index,⁵⁷ D , is a physical parameter which is often used^{58–61} to quantify the degree of bond length distortion of coordinated species around a central ion. It is defined as:

$$D = \frac{1}{n} \sum_{i=1}^n \frac{|l_i - l_{\text{av}}|}{l_{\text{av}}} \quad (2)$$

where l_i is the distance between the core ion and the i th coordinated ion, and l_{av} is the average of all the distances between the core ion and coordinated ions. We here calculate a $D = 0.01320(12)$, which is similar to that previously reported for mixed $\text{Mn}^{3+/4+}\text{O}_6$ octahedra (with an average oxidation state of $\sim 3.42+$) in $\text{Pb}_3\text{Mn}_7\text{O}_{15}$.⁵⁹ We can compare the

absence of a cooperative Jahn–Teller distortion to mixed-valent $\text{Mn}^{3+/4+}$ system LiMn_2O_4 spinel which, even with a much larger Mn^{3+} fraction ($\sim 50\%$, corresponding to a mean valence $+3.5$) than the cryptomelane sample studied here, does not exhibit Jahn–Teller order. However, Jahn–Teller order onsets on electrochemical lithiation towards $\text{Li}_2\text{Mn}_2\text{O}_4$ with a transition from cubic to tetragonal symmetry⁶² as mean Mn valence approaches $+3$. This suggests that, with a mean Mn valence of $+3.779(2)$, the Mn^{3+} fraction in our sample of $\text{K}_{1.448(3)}\text{Mn}_8\text{O}_{16}$ is simply too low to drive long-range cooperative Jahn–Teller order.

Low-temperature synchrotron diffraction

Variable-temperature synchrotron diffraction was performed on cooling from 300 K to 100 K to examine the low-temperature crystal structure of cryptomelane. A tetragonal symmetry was observed on cooling from room-temperature to T_1 , although a continuous increase in anisotropic peak broadening can be seen [Figure S16]. T_1 was observed to occur at ~ 175 K, below which two significant changes associated with the cryptomelane phase occurred. Firstly, diffraction peaks began to broaden and even split [Figures S10(b) and S9(e)], suggesting that the average structure is lowered due to a subtle monoclinic distortion, similar to that reported by Boschetti *et al.*⁵² Secondly, a series of weak superlattice peaks appeared (at $d = 7.35 \text{ \AA}$, 3.37 \AA , 3.03 \AA , and 2.58 \AA), consistent with a non-magnetic structural modulation [Figure S9].

The diffraction data at 100 K cannot be satisfactorily fit using a tetragonal $I4/m$ cell, and so a monoclinic $C2/m$ (space group #12) cell derived from a distortion of the $I4/m$ structure was used for Rietveld refinement [Figure S11; Table S4]. This model does not account for the superlattice peaks, however, which cannot be indexed to any commensurate modulation of either the monoclinic or tetragonal cell. We then performed a sequential Rietveld refinement of the diffraction data to evaluate the nature of the monoclinic distortion and the tetragonal \leftrightarrow monoclinic transition. We describe the monoclinic unit cell in terms of pseudo-tetragonal lattice parameters, given by:

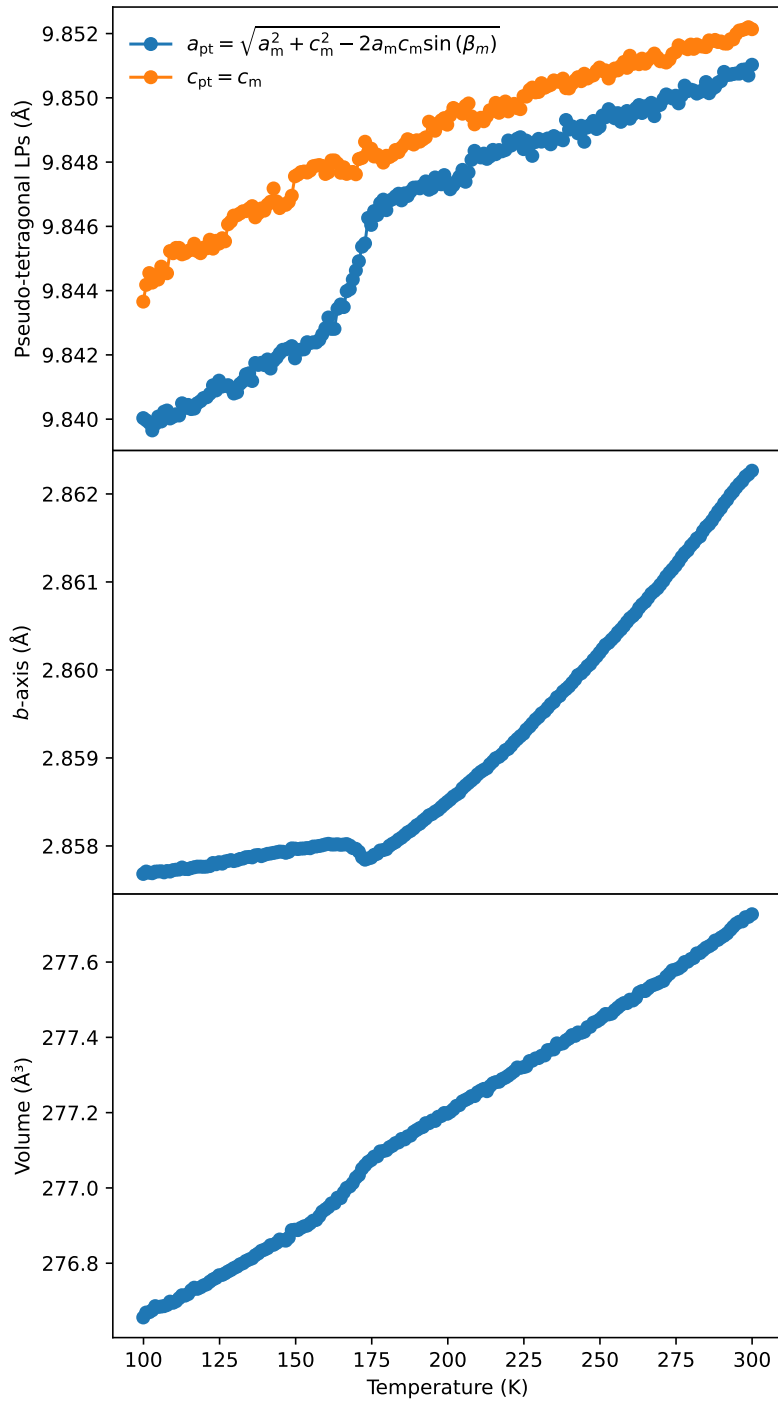


Figure 3: Top: Pseudo-tetragonal lattice parameters, a_{pt} and c_{pt} (Eqs 3 and 4); middle: lattice parameter b parallel to nanotunnels; bottom: unit cell volume, all as a function of temperature. Data obtained from sequential Rietveld refinement of synchrotron diffraction data. Temperature dependence of original monoclinic lattice parameters shown in Figure S12.

$$a_{\text{pt}} = \sqrt{a_{\text{m}}^2 + c_{\text{m}}^2 - 2a_{\text{m}}c_{\text{m}} \sin \beta} \quad (3)$$

$$c_{\text{pt}} = c_{\text{m}} \quad (4)$$

where we use a setting in both cases where $b_{\text{m}} = b_{\text{pt}}$ is the direction parallel to the tunnels. Figure 3 shows the temperature dependence of these lattice parameters. Around 100 K the two pseudo-tetragonal distances are clearly distinct, but they appear to approximately converge at T_1 ; this, along with the monoclinic β converging on the high-symmetry value of 135° [Figure S12] support the interpretation that T_1 is the tetragonal \leftrightarrow monoclinic transition. Additionally, we also see a crossover in the magnitude of fit quality (given by R_{wp}) for sequential Rietveld refinements performed using a tetragonal and monoclinic unit cell [Figure S24], with the monoclinic model giving a better fit below T_1 and the tetragonal model giving a better fit above T_1 .

Thermal expansion is highly anisotropic in both temperature regimes [Figure S14]. In the $100 \text{ K} < T < T_1$ regime, there is very little expansion parallel to the nanotunnels ($\sim 0.02\%$) compared with that in the pseudo-tetragonal axes ($\sim 0.06\%$). Conversely, in the $T_1 < T < 300 \text{ K}$ regime, there is an increase of $\sim 0.15\%$ in the b -axis compared with an increase of $\sim 0.03\%$ (as a percentage of magnitude at 100 K) between T_1 and 300 K.

In the room-temperature structure there was a single Mn site, whereas in the monoclinic cell there are two Mn sites, both with Wyckoff $4i$ ($x, 0, z$) symmetry: Mn1 and Mn2. We calculate the BVS (using Equation 1) for each of these sites in Figure S23, and find radically different valences for each site, calculating 3.37(3) and 4.14(5), respectively for Mn1 and Mn2 at 100 K. This suggests that Mn2 is entirely in the Mn^{4+} oxidation state, whereas Mn1 consists of a mixture of the $\text{Mn}^{4+}/\text{Mn}^{3+}$ oxidation states. While the distribution of $\text{Mn}^{4+}/\text{Mn}^{3+}$ on the Mn1 site may be entirely random, it is plausible that there may be some incommensurate ordering of $\text{Mn}^{4+}/\text{Mn}^{3+}$ on the Mn1 sublattice giving rise to the weak

incommensurate reflections which emerge below T_1 .

As in the room-temperature tetragonal structure, each MnO_6 octahedron in the monoclinic structure has four unique Mn-O bond lengths: two are opposite one another, the other two unique bond lengths occur within the same plane, with equal-length bonds occurring 90° from one another. Calculation of bond length distortion index⁵⁷ [Figure S21] gives a value (0.0283(12)) for Mn1 which is 3 times larger than for Mn2 (0.0116(11)) at 100 K. This is consistent with Mn2 having a non-Jahn-Teller active 4+ oxidation state, while Mn1 appears to be a mixture of Mn^{3+} and Mn^{4+} , potentially resulting in JT character. The distortion index value for Mn1 is still small compared with that of Jahn-Teller-distorted NiO_6 octahedra in NaNiO_2 (0.05463(14))⁶⁰ or MnO_6 octahedra in CuMnO_2 ,⁵⁸ but is comparable to mixed-valent MnO_6 octahedra in $\text{Pb}_3\text{Mn}_7\text{O}_{15}$.⁵⁹ We also consider the polar O-O distances in each octahedron, Figure S22, and see that there are two short and one long distance for each octahedron consistent with a partial Jahn-Teller distortion, although for Mn2 a high bond angle variance [Figure S21] is the likely reason for the smaller O-O bond length. We therefore conclude that it is plausible that there is a Jahn-Teller distortion on the Mn1 site based on the signatures of a tetragonal octahedral elongation, but the presence of multiple competing geometric constraints on the octahedron and the mixed-valence nature of this site make it impossible to definitively attribute site distortion to the Jahn-Teller effect.

Magnetometry and heat capacity

The magnetic transitions in our sample of $\text{K}_{1.448(3)}\text{Mn}_8\text{O}_{16}$ cryptomelane were studied using DC and AC magnetic susceptibility, heat capacity and isothermal magnetisation. We observe each of the three transitions which have previously been observed in K-rich cryptomelane. Here we follow the notation of Ref. 17, labelling the transitions as T_1 , T_2 , and T_3 in descending order of temperature.

Figure 4(a) shows T_2 and T_3 in the magnetic susceptibility χ , $\frac{d\chi}{dT}$, and magnetic heat capacity as a function of temperature, and Figure 4(b) shows T_1 in the inverse magnetic

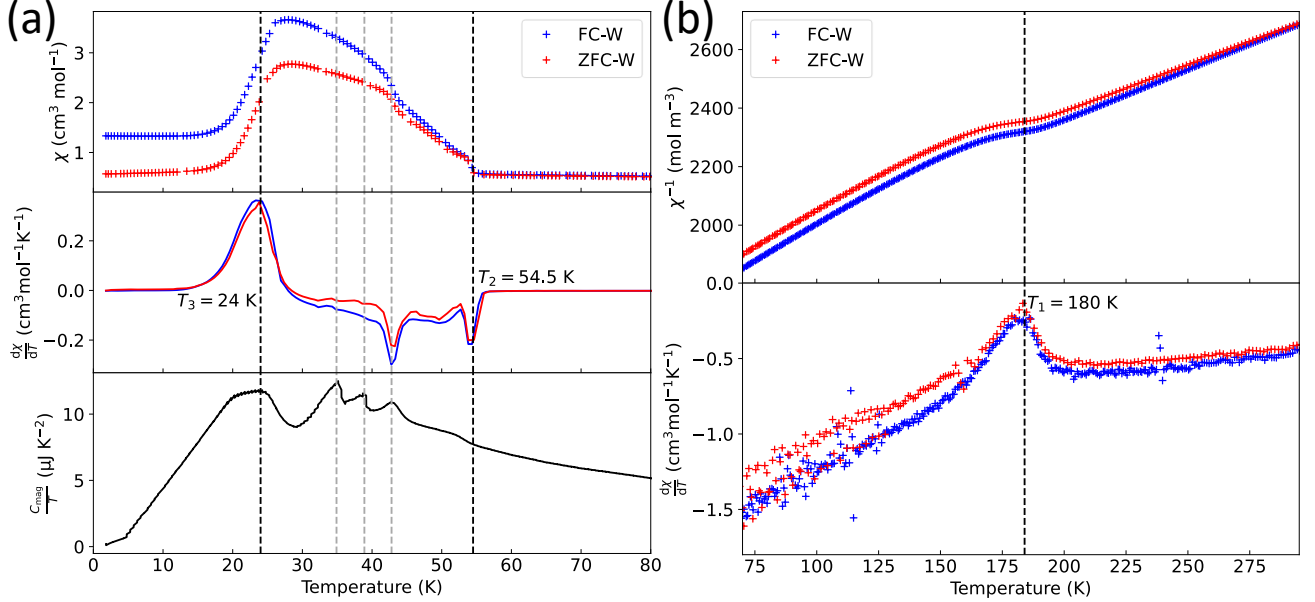


Figure 4: (a) Magnetic susceptibility χ , $d\chi/dT$, and heat capacity as a function of temperature. (b) Inverse magnetic susceptibility and $d\chi/dT$ as a function of temperature in the vicinity of T_1 . Vertical dashed lines indicate where transition temperature values are assigned; black lines are due to cryptomelane and grey lines are due to Mn_3O_4 .^{63–66} ZFC-W and FC-W denote zero-field-cooled and field-cooled measurements, measured during warming in a field of 200 Oe.

susceptibility and $\frac{d\chi}{dT}$. The precise values assigned to these transitions are determined from the plot of $\frac{d\chi}{dT}$ against temperature: $T_1 = 184$ K, $T_2 = 54.5$ K, and $T_3 = 24$ K. The other transitions observed in the heat capacity and magnetic susceptibility at 34.9 K, 38.9 K, and 42.8 K are all associated with magnetic ordering of Mn_3O_4 as has been described in the literature.^{63–66} Fitting the Curie-Weiss law⁶⁷ to our data in the range 200 K to 300 K yields effective moment $\mu_{\text{eff}} = 5.00(4) \mu_B$ for the ZFC-W susceptibility data and $4.80(3) \mu_B$ for the FC-W susceptibility data, along with Weiss constants of $-483(6)$ K and $-550(10)$ K, respectively. This effective moment exceeds what we would expect for a mixed- $\text{Mn}^{3+/4+}$ system with this stoichiometry ($\sim 4.1 \mu_B$), and any discrepancy is likely due to the fact that our fitting range is below the modulus of the Weiss constant where there are likely some persistent magnetic correlations.

The value of T_1 at 184 K, occurs within the range of previously-reported values.^{17,19} Reported values of T_2 and T_3 vary over a broad range. Our values of $T_2 = 54.5$ K and $T_3 = 24$ K

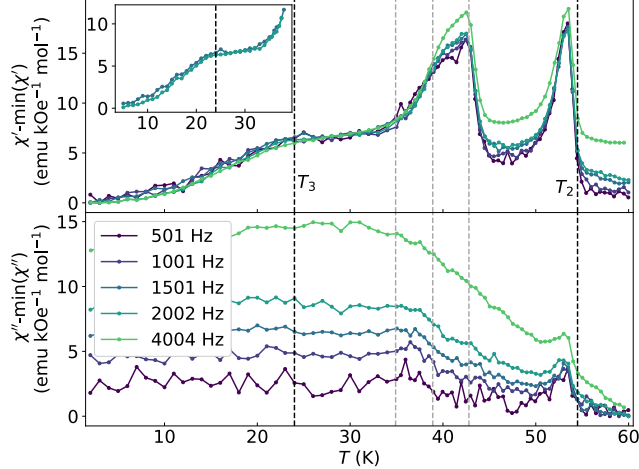


Figure 5: Variable -temperature and -frequency AC susceptibility measurements at 501 Hz, 1001 Hz, 1501 Hz, 2002 Hz, and 4004 Hz, shown in terms of the real χ' (top) and imaginary χ'' (bottom) components of the overall AC susceptibility. The inset shows the data for 1501 Hz and 2002 Hz only, with a focus on the T_3 transition. Positions of vertical lines match those in Figure 4.

are slightly higher than most previous studies. Barudžija *et al.* report a T_2 transition of either 49 K or 51 K (sample-dependent)²² and Sato *et al.* report 52 K.¹⁷ For T_3 , these works report 21 K or 20 K, and 20 K respectively. This may be due to our defining the transition by the maximum in $\frac{d\chi}{dT}$, rather than the peak in the $\chi(T)$. Additionally, although there is ostensibly a very similar K^+ content, our work calculated K^+ content based on Rietveld refinement whereas the referenced works^{17,22} calculate K^+ content based on ratio of precursors. Consequently, there may be a discrepancy in stoichiometry. A theoretical study¹³ shows a dependence of transition temperature on the degree of K^+ cation content, and so it is unsurprising that the range of reported temperatures is fairly broad. In our sample, there is divergence between measurements performed after cooling with/without an external magnetic field (FC-C/ZFC-C, respectively), which has previously been interpreted as evidence of spin glass-like ordering;^{22,23} this divergence is present at all measured temperatures (below 300 K) but becomes significant below T_2 .

AC susceptibility measurements between 2 K and 60 K are presented in terms of their real χ' and imaginary χ'' components in Figure 5. T_2 manifests as a large feature in both

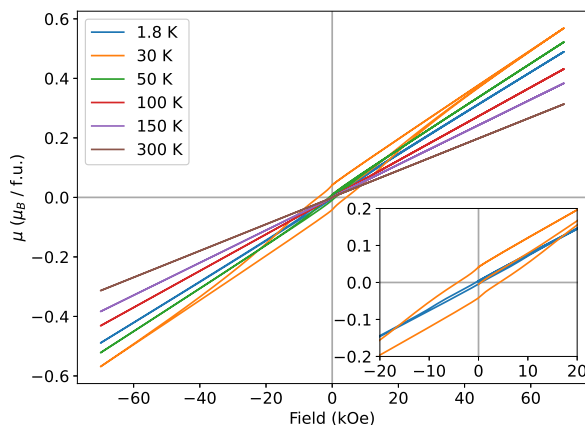


Figure 6: Fixed-temperature field-dependent magnetisation measurements at 1.8 K, 30 K, 50 K, 100 K, 150 K, and 300 K, showing moment per formula unit of $\text{K}_{1.448(3)}\text{Mn}_8\text{O}_{16}$. Inset: 1.8 K and 30 K field-dependent magnetisation data, zoomed in to highlight the different hysteretic behaviour.

the real and imaginary susceptibility data, peaking around 53.5 K; this has been reported by Barudžija *et al.*^{22,23} in AC studies on K_xMnO_2 with similar composition. There is a more subtle shoulder for T_3 in our AC χ' , but no feature can be resolved for χ'' . Additionally, the incommensurate ordering of Mn_3O_4 around 43 K is present in our data as a large feature in χ' .

Finally, isothermal DC susceptibility measurements are shown in Figure 6. At 1.8 K, there is negligible hysteresis, suggesting there is no ferro- or ferri-magnetic behaviour for $T < T_3$. However, at 30 K and, to a lesser extent, 50 K, there is magnetic hysteresis. This suggests that for $T_3 < T < T_2$ there is a ferro- or ferri-magnetic component to the magnetic structure. This is consistent with the previous reports.^{17,24}

Magnetic ordering from neutron diffraction

Variable temperature neutron diffraction was measured on the D20 instrument at ILL, Grenoble [SI Figure S3]. Measurements were collected in the range 2.5 K to 60 K in order to study the changes on cooling through T_2 and T_3 . Difference patterns are shown in Figure 7, in which

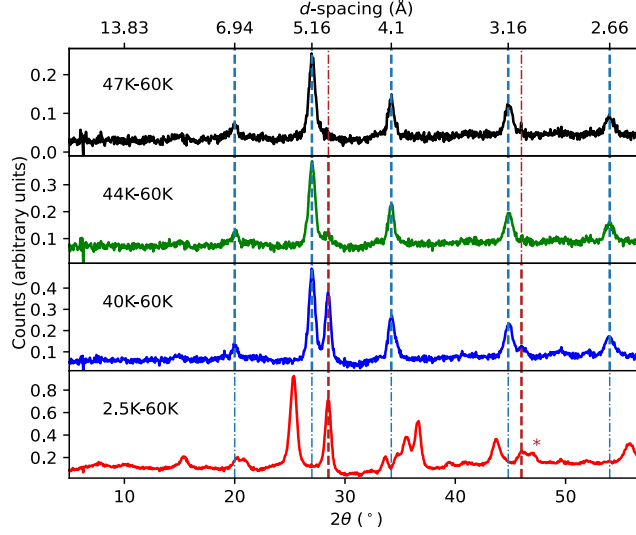


Figure 7: Experimental diffraction difference patterns X K-60 K ($X=47$ K, 44 K, 40 K, and 2.5 K). Blue dashed vertical lines indicate peaks associated with the commensurate $\vec{k}_{\text{mag}} = 0$ and incommensurate $\vec{k}_{\text{mag}} = (0, \sim 0.37, 0)$ components for $T_3 < T < T_2$. Dark red dashed vertical lines and asterisks show peaks associated with magnetic ordering in Mn_3O_4 . The vertical lines are thick at the temperatures where the associated peaks are present, and thin at temperatures where they are not.

the diffraction data at 60 K (with no magnetic diffraction peaks) are subtracted from the lower-temperature diffraction patterns, to allow magnetic Bragg peaks to be readily identified. The changes in pseudo-tetragonal lattice parameters are continuous over the measured temperature points, and all lattice parameters decrease with cooling. The emergence of new peaks in neutron diffraction below $T_2 = 54.5$ K are consistent with magnetic ordering.

Some emergent peaks in these diffraction patterns can be assigned to the two impurity phases. For all of the low- T diffraction patterns, a peak at 14.7° ($d \approx 9.4$ Å) is present, becoming most prominent at the lowest measured temperature; this may be the [100] magnetic peak of Mn_2O_3 ,^{68,69} although Mn_2O_3 has a very small (0.049(5)%) refined phase fraction at room temperature.

Additional magnetic Bragg peaks due to magnetic ordering of the 2.8(3)wt% Mn_3O_4 impurity are observed. At 40 K and 2.5 K, peaks at $\sim 28.4^\circ$ ($d = 4.9$ Å), 34.7° ($d = 4.04$ Å; little more than a shoulder at 40 K), and $\sim 46^\circ$ ($d = 3.08$ Å) are attributed to the [101],

[110], and [112] reflections respectively.^{63–66} At 2.5 K, Mn_3O_4 has extra Bragg peaks due to its magnetic transition at 33 K.^{63–66}

We assume all other emergent peaks are attributable to the cryptomelane phase. The following two sections will detail our analysis of the $T_3 < T < T_2$ regime (which we study at 47 K which is in the paramagnetic regime of Mn_3O_4) and the $T < T_3$ magnetic regime. Due to the low resolution of the neutron data compared with that of the synchrotron, the subtle monoclinic distortion cannot be resolved in this data. We still perform magnetic analysis using the monoclinic structure, but present alternative analysis using the tetragonal structure in SI Section 9; the results are equivalent for the incommensurate cell, but the commensurate cell shows clear differences with the symmetry change as will be discussed.

Magnetic structure for $T_3 < T < T_2$

At 47 K, five clear magnetic Bragg peaks are observed in the difference pattern [Figure 7]. Only one of the main magnetic peaks, at $d = 6.95 \text{ \AA}$, can be assigned to a commensurate magnetic structure, with propagation vector $\vec{k}_{\text{mag}} = (0, 0, 0)$. This peak corresponds to the nuclear [110] Bragg peak in the tetragonal basis, or a superposition of the [001] and $[20\bar{1}]$ reflections in the monoclinic unit cell. The remaining four peaks ($d = 5.15, 4.10, 3.15, 2.65 \text{ \AA}$) can only be indexed to a propagation vector incommensurate with the crystal structure, $\vec{k}_{\text{mag}} = (0, k_y, 0)$ [$k_y \approx 0.3687$] (where we here use a monoclinic cell with special b -axis).

For each propagation vector, there are multiple symmetry-allowed IRs. The correct IR would describe the basis vector behaviours at each magnetic site, which collectively make up the magnetic structure. There are 2 possible IRs for $\vec{k}_{\text{mag}} = (0, \sim 0.37, 0)$ and 4 IRs for $\vec{k}_{\text{mag}} = (0, 0, 0)$ in a $C2/m$ cell with magnetic ions on the $4e$ Wyckoff site; these are denoted using Γ_i^j ($i = 1, 2, 3, \text{ or } 4$; $j = \text{IC or C}$ where IC/C stands for InCommensurate or Commensurate). The basis vectors (BVs) are tabulated in Section VII of Supplementary Information. We then use magnetic Rietveld refinement to test the IRs against the experimental difference pattern (47 K-60 K), shown in Figure 9 and determine the magnetic structure.

Of the four IRs for the commensurate component, Γ_1^C and Γ_3^C give a net moment, and Γ_2^C and Γ_4^C do not (see Table S6 of SI). As we know from magnetometry that there is a net moment in the $T_3 < T < T_2$ regime, and this net moment must come from the commensurate component of the magnetic structure, we only consider Γ_1^C and Γ_3^C as possible IRs. We then consider prior experimental work on $K_{1.5}(\text{H}_3\text{O})_x\text{Mn}_8\text{O}_{16}$ single crystals which indicate that the magnetic hysteresis is much stronger in the plane perpendicular to the tunnels than along the tunnels.¹⁷ On this basis, we then rule out Γ_1^C , leaving only Γ_3^C as a viable candidate for the commensurate component of the magnetic structure. In this IR, all moments are parallel for a given site. From preliminary analysis, there appears no improvement in the fit from decoupling the moments on the two Mn sites in this $|\vec{k}_{\text{mag}}| = 0$ structure, so we constrain the moments on both Mn sites to be equal in magnitude. We find that: (1) fit quality is entirely independent of the direction of the net moment within the plane perpendicular to the tunnels, and (2) refining the basis vectors in the [100] and [001] directions independently leads to divergence within FULLPROF. This is due to the fact that, to the low resolution of the neutron diffraction data, the monoclinic splitting cannot be resolved and therefore our cell is pseudo-tetragonal; in a tetragonal cell, moments direction in the basal plane cannot readily be determined using powder diffraction data. For this reason, we arbitrarily constrain the net moments in the a and c -directions to be equal; we do not assert that net moment must occur in the [101] direction for the commensurate component however because a [100] or [001] net moment would also be consistent with the available data. For completeness, we note that the analysis using a tetragonal cell (Section S9) yields a similar commensurate component to that found with the monoclinic cell.

For the incommensurate $\vec{k}_{\text{mag}} = (0, \sim 0.37, 0)$, it is possible to obtain a reasonable fit to the incommensurate peaks in the experimental diffraction data with Γ_2^{IC} , but not with Γ_1^{IC} . We first tested a Γ_2^{IC} model assuming sinusoidal modulation of moments along the nanotunnels, which yields a good fit [SI Figure S27]. However, we noted that there appeared no dependence whatsoever of fit quality on the plane in which moments are allowed to

oscillate sinusoidally; as with the invariance of fit quality with moment direction for the commensurate case, this is a consequence of symmetry. This observation, combined with the prior experimental and theoretical works which indicate helical ferrimagnetism in this temperature regime,^{16,17,20} led us to test a helical model in which constant moments rotate about the propagation vector with period equal to b/k_y . This was achieved by representing moments as spherical coordinates, and configuring a 180° phase shift between the two Mn sites to ensure that the structure was equivalent to Γ_2^{IC} . The resulting fit is shown in Figure 9 and the associated magnetic structure is shown in Figure 8(b).

While the coexistence of two possible IRs may indicate magnetic phase segregation into two phases each with one of these two IRs, we do not consider this as likely in this context. Firstly, given that the sample has multivalent Mn, magnetic phase segregation would probably correspond to segregation of Mn^{3+} and Mn^{4+} which would be identifiable as phase segregation in high-resolution synchrotron diffraction. Secondly, such a scenario would indicate an entirely ferromagnetic phase due to the commensurate component, which is difficult to envisage given that the ground state of $\alpha\text{-MnO}_2$ is antiferromagnetic.⁷⁰ Additionally, we note that coexistence of a $|\vec{k}_{\text{mag}}| = 0$ and $|\vec{k}_{\text{mag}}| \neq 0$ component is not uncommon in magnetic structures.^{71,72} We therefore consider it likely that both IRs coexist over the bulk of the sample, and hence fit the scale factors $S_C = S_{\text{IC}} = S_{\text{crystal}}$ from which the refinement determines the magnitude of each moment at 47 K for the commensurate component to be $0.320(16) \mu_{\text{B}}$, and the magnitude of the individual moments in the incommensurate component (assuming purely helical modulation) to be $0.513(4) \mu_{\text{B}}$. The net magnitude of each individual moment would result from the superposition of the commensurate and incommensurate components; at 47 K, the magnitude for each moment occurs in the range $0.513(4) \pm 0.320(16) \mu_{\text{B}}$ depending where along the modulation the moment occurs. We note here that at 47 K the magnetization is far from being saturated as can be clearly seen from Figure 4(a), which is why the moment magnitudes are smaller than the fully saturated moments expected for $\text{Mn}^{3+}/\text{Mn}^{4+}$. The obtained moment from the commensurate component

appears approximately consistent with that obtained from the fixed-temperature, variable-field magnetometry measurement [Figure 6], although as the moment doesn't saturate it is difficult to be certain.

We note that we observe no dependence of the propagation vector on temperature in the incommensurate magnetic component between 40 K and 47 K [Figure S6], and so it is unlikely there are any qualitative changes in the magnetic structure within this temperature regime.

Magnetic structure for $T < T_3$

For $T < T_3$ we only have one diffraction pattern, at 2.5 K. There are many more peaks in the 2.5 K-60 K difference pattern than in the 47 K-60 K difference pattern, although the peaks due to the $\vec{k}_{\text{mag}} = (0, \sim 0.37, 0)$ component disappear entirely (see Figure 7). This increase in the number of peaks is in part due to the magnetic ordering of Mn_3O_4 , which exhibits several additional magnetic peaks due to its commensurate magnetic structure below ~ 33 K.⁶³⁻⁶⁶ Additionally, we assign the peak at 14.7° ($d \approx 9.4 \text{ \AA}$) to the [100] magnetic peak of Mn_2O_3 .^{68,69} Despite this, most of the peaks are not attributable to a known impurity and are therefore attributed to a new magnetic ordering in cryptomelane.

It should be noted here that it has been reported that at low temperatures, the impurity phase Mn_3O_4 exhibits some structural phase separation, with a fraction of it exhibiting an orthorhombic structure as opposed to its usual tetragonal structure.^{66,73,74} However, such effects are too subtle to observe when Mn_3O_4 is a minor impurity, and we do not include the reported orthorhombic phase in our analysis.

Similarly to $T_3 < T < T_2$, the majority of the magnetic peaks for $T < T_3$ cannot be indexed to a commensurate magnetic unit cell. However, the nuclear [110] and [220] Bragg peaks do increase in intensity at 2.5 K compared with 60 K, and so it is likely that, as is the case for $T_3 < T < T_2$, there is a commensurate component to the magnetic ground state. Unlike the higher-temperature commensurate component, such a component cannot

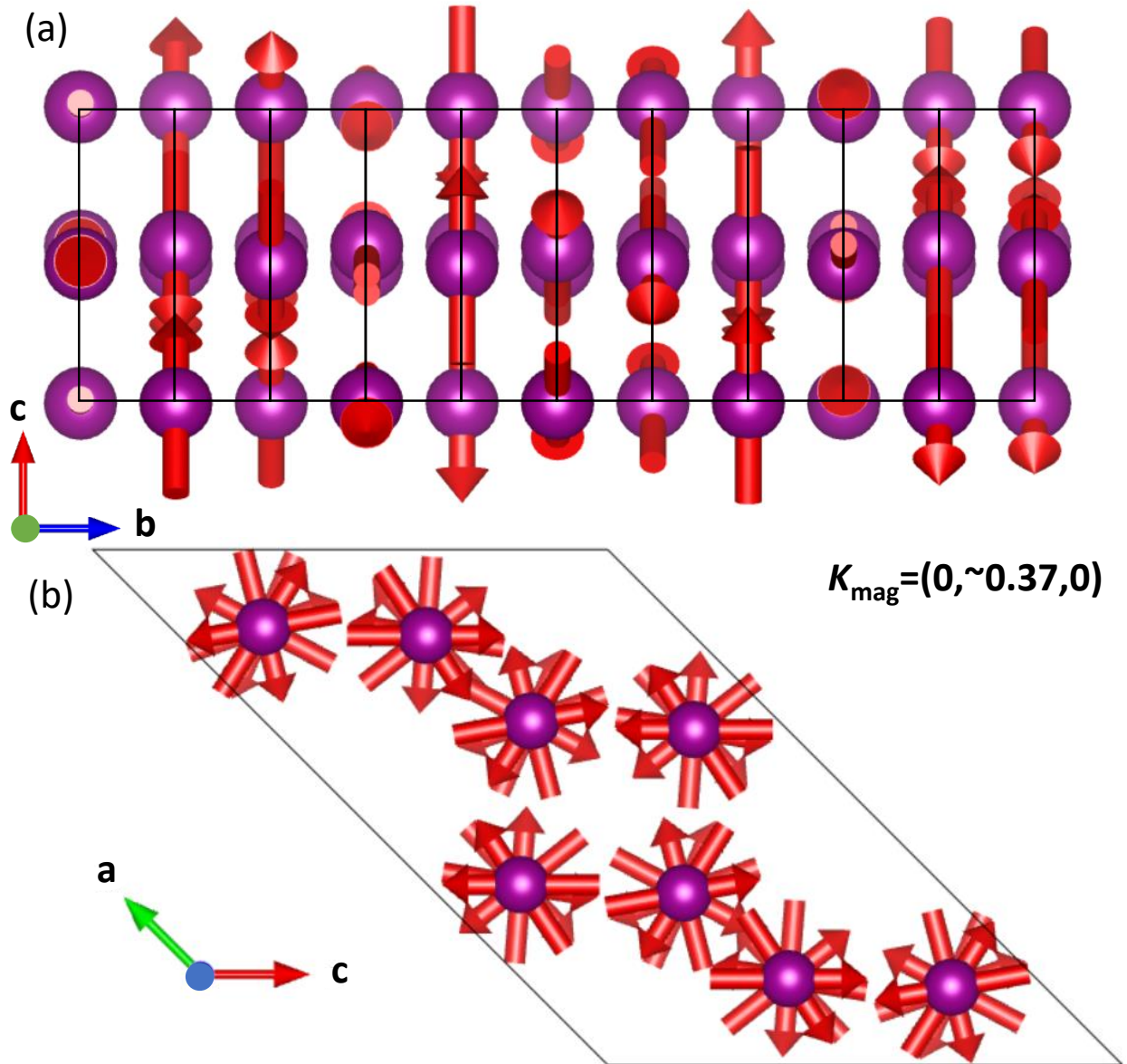


Figure 8: The refined magnetic unit cell for the incommensurate $\vec{k}_{\text{mag}} = (0, \sim 0.37, 0)$ components of the magnetic structure for $T_3 < T < T_2$ assuming a monoclinic ($C2/m$) unit cell, assuming a helical ordering. (a) View perpendicular to nanotunnels, (b) view along nanotunnels.

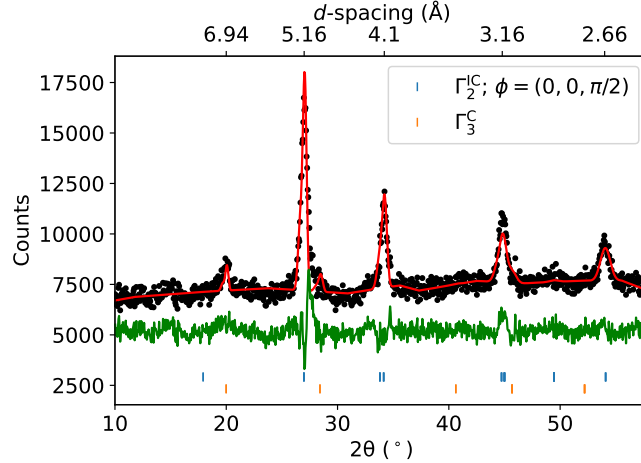


Figure 9: Experimental difference pattern 47 K-60 K, compared with calculated pattern obtained by Rietveld refinement of the model for $T_3 < T < T_2$, consisting of a commensurate $|\vec{k}_{\text{mag}}| = 0$ and incommensurate $\vec{k}_{\text{mag}} = (0, \sim 0.37, 0)$ component, assuming a monoclinic ($C2/m$) unit cell. The incommensurate structure was represented with a helical model, with moments only in the plane perpendicular to the propagation vector. We note that a fit of comparable quality can be obtained by substituting the incommensurate component with either a sinusoidal modulation in monoclinic symmetry [SI Figure S27], an ellipsoidal helix [Figure S29], or a constant-moment helix assuming tetragonal ($I4/m$) symmetry [SI Figure S30].

have a net moment, as inferred from the lack of hysteresis for $T < T_3$ from the fixed-temperature variable-field magnetisation measurements [Figure 6]. The commensurate component is therefore likely to be described by either Γ_2^C and Γ_4^C [Table S6].

Excluding these commensurate peaks, we have attempted to index the remaining peaks. However, we have not been able to find a single incommensurate propagation vector with fewer than 3 incommensurate components which leads to all additional peaks being fit. We note that $\vec{k}_{\text{mag}} = (0, \sim 0.15, 0)$ is able to fit some of the additional peaks, but not all. This means that either the propagation vector is incommensurate in 3 spatial dimensions, or that there are multiple incommensurate propagation vectors. Both of these possibilities are difficult to test with neutron powder diffraction alone, and single-crystal studies are required. Consequently, we are not able to solve the magnetic structure for $T < T_3$, but we can say that it is more complex than for $T_3 < T < T_2$ and that it has magnetic Bragg peaks inconsistent with a spin glass-like state.

Discussion

To understand the magnetic properties of a material, it is important to understand the nature of the exchange interactions. For J_1 and J_2 interactions it is unlikely there is direct exchange given the large interatomic distances relative to the Shannon radii⁷⁵ of Mn^{3+} and Mn^{4+} . Given the presence of both Mn^{3+} and Mn^{4+} , rationalizing the nature of the interactions using the Goodenough-Kanamori-Anderson rules⁷⁶⁻⁷⁸ is non-trivial.¹³ This is further complicated by the possibility for double exchange; whilst the Mn-O-Mn angles deviate from 90° , double exchange has been discussed in other mixed valent materials with non- 90° M -O- M ($M =$ transition metal) bond angles, such as rutile chains.⁷⁹

Our finding that the magnetic ordering length-scale is incommensurate with the lattice parameters in $\text{K}_{1.448(3)}\text{Mn}_8\text{O}_{16}$ is in keeping with prior literature for doped- and undoped- α - MnO_2 . For example, a theoretical study on the undoped variant using a Heisenberg model²⁰ does indeed predict helical ordering. The prediction in the study²⁰ requires the angle of helical rotation of spins per lattice parameter, ϕ , to meet the condition $\pi/2 < \phi < \pi$, which in our case it does, as $\phi \approx 0.37 \cdot 2\pi = 0.74\pi$. This places the observed incommensurate modulation within the helical regime predicted for frustrated interactions on the hollandite lattice, supporting a qualitative correspondence between the theoretical model and the experimentally observed modulated magnetic order for $T_3 < T < T_2$.

There is also a strong correspondence between our work and the helical ferrimagnetism model proposed by Sato *et al.*^{16,17} for $\text{K}_{1.5}(\text{H}_3\text{O})_x\text{Mn}_8\text{O}_{16}$. In this model, there are modulated spin and charge behaviours with length-scales λ_m and λ_c respectively, along the crystallographic axis of the tunnels. The modulated charge behaviour is due to mixed valent $\text{Mn}^{3+}/\text{Mn}^{4+}$. The charge modulation will determine the magnitude, and the spin modulation will determine the orientation, of individual spins. For a normal helical magnetic system, there will be no net moment. However, with this combination of charge and spin modulations, it is argued that when $\lambda_c/\lambda_m = n$ (n being any integer), there will be a slight net magnetic moment. Sato *et al.* hypothesise that for $25 < T < 55$ K, n is an integer, and the

transition at $T \approx 25$ K results in n no longer having an integer value, hence the lack of a net moment below this temperature. This model, for $T_3 < T < T_2$, would be best represented in terms of propagation vectors by a dual- \vec{k} model with $\vec{k}_{\text{mag}} = (0, k_y, 0)$ and $\vec{k}_{\text{mag}} = (0, 0, 0)$, which is precisely what we show. Assuming charge-ordering length $\lambda_c = 8b$ (where b is the lattice parameter along the tunnel axis), $\lambda_c/\lambda_m = 8 \cdot 0.37 \approx 3$ for $k_y = 0.37$, which is precisely the condition they propose for a slight net magnetic moment. Additionally, our isothermal and variable-temperature DC susceptibility measurements resemble those reported.^{16,17} Our work therefore supports the helical ferrimagnetism model of Sato *et al.*^{16,17} Experimentally, a similar incommensurate magnetic order has been reported for rutile β - MnO_2 ⁸⁰ based on neutron diffraction, and attributed to Sato *et al.*'s^{16,17} helical ferrimagnetism model.

Crespo *et al.*¹³ show theoretically that the α - MnO_2 crystallographic motif with inhomogeneous doping may exhibit spin glass behaviour in the presence of antiferromagnetic exchange interactions in an Ising spin lattice. Previous experimental works on K-rich cryptomelane have indicated that T_3 may be a spin glass-like transition.^{22,23} From our DC and AC susceptibility measurements, we see an FC/ZFC divergence which could support this. However, we do not see a strong frequency dependence to the magnetic behaviour [Figure 5] which is a characteristic feature of a spin glass.^{81–86} Furthermore, the magnetic Bragg peak structure we see for $T < T_3$ is not consistent with spin glass-like ordering, as a spin glass phase would not exhibit magnetic Bragg peaks.⁸³ The proposed transition to a spin glass-like state is therefore not supported by our data, and if such a state is present in K-rich cryptomelane of the stoichiometry studied here, then it is constrained to be an extrinsic phenomenon: either a surface effect, or resulting from variation in K^+ content across the bulk sample. The possibility that spin glassiness is a surface phenomenon has been suggested for similar materials, including $\text{Na}_{2-x}\text{Mn}_8\text{O}_{16}$ ⁴ and $\text{Ba}_{1+\delta}\text{Mn}_8\text{O}_{16}$.⁸⁷ The second possibility that a spin glass is caused by variations in local K^+ content within some regions of the sample is also highly plausible; it is already known that spin glass-like behaviour occurs for $\text{K}_x\text{Mn}_8\text{O}_{16}$ ($x < 1$),^{15,18,19} and it has also been shown that Sn-doping of α - MnO_2 results in

spin glass-like behaviour.² Therefore, we suggest that our observed magnetic Bragg peaks for $T < T_3$ may be reconcilable with previous claims of spin glassiness, but that such a spin glass-like state cannot be the bulk ground state of $\text{K}_{1.448(3)}\text{Mn}_8\text{O}_{16}$.

Our findings of magnetic Bragg peaks in both temperature regimes is consistent with the only known previous neutron diffraction study on $\text{K}_{1.72}\text{Mn}_8\text{O}_{16}$.²⁴ However, the magnetic peak positions do not match those in this study, with the result that our magnetic structure solution is unlikely to be the structural solution for their reported data, although there is the possibility for a $\vec{k}_{\text{mag}} = (0, 0, 0)$ component from their data, as for ours. This indicates that there is a strong sample dependence of the magnetic propagation vector(s), which should be studied further in future work.

The first magnetic ordering temperature of cryptomelane, at around 55 K, is around 10% the value of the Weiss constant we obtained from Curie-Weiss fitting. This means the magnetic ordering occurs at a far lower energy scale than that of the magnetic interactions, suggesting that the ordering is inhibited by the frustrated magnetic interactions present in the Mn sublattice of the crystal structure. From this we can conclude that frustration likely plays a role in the magnetism, an inference further supported by the spin reorientation around 25 K. There are parallels with this in the literature; for instance, MgCr_2O_4 ⁸⁸ and $\text{LiInCr}_4\text{O}_8$ ⁸⁹ spinels, and $\text{CaMn}_7\text{O}_{12}$,⁴⁹ are frustrated systems exhibiting two co-existing propagation vectors. The presence of multiple propagation vectors is likely a consequence of these competing interactions with large energy scales.

In addition to the incommensurate magnetic ordering, we also observed the emergence of incommensurate structural ordering below T_1 . We were unable to solve the incommensurate structural ordering, due to the complexity of the peak structure and the absence of single-crystal diffraction data. One hypothesis for the origin of these peaks is that the incommensurate structural ordering is a $\text{Mn}^{3+}/\text{Mn}^{4+}$ charge ordering phenomenon, which would be consistent with the model of Sato *et al.* described earlier.¹⁶ Alternative explanations for the incommensurate reflections may be: (1) that the K^+ cations, randomly distributed

and highly mobile at room temperature, freeze into regular but incommensurate positions along the nanotunnels at low temperature, or (2) that there is an incommensurate MnO_6 octahedral tilt ordering. It is also possible that some or all of these phenomena occur simultaneously. Incommensurate structural ordering has been observed in other materials, including tetragonal bronzes,^{90–95} perovskites,^{96–98} and A_2BX_4 layered structures.^{99,100}

Conclusion

We have studied the structural and magnetic properties of cryptomelane, $\text{K}_x\text{Mn}_8\text{O}_{16}$ with precise composition $x = 1.448(3)$. We have found that, structurally, the previously reported transition T_1 corresponds to a structural transition: below this temperature, there emerges a subtle monoclinic distortion from the high-temperature tetragonal aristotype, and an incommensurate structural ordering with unknown origin. Examining the magnetic properties, we find that there are two distinct ordered magnetic regimes in the temperature ranges $T < 24$ K and $24 < T(\text{K}) < 54.5$. For $T < 24$ K, the sample has bulk magnetic ordering, so any spin glass component in the sample is either due to surface effects or is a local phenomenon within some regions of the sample. For $24 < T < 54.5$ K, there is an incommensurate propagation vector $\vec{k}_{\text{mag}} = (0, k_y, 0)$ [$k_y = 0.3690(2)$], which is likely helical in the ab -plane, along with a commensurate magnetic cell which we successfully fit with a $\vec{k}_{\text{mag}} = (0, 0, 0)$ propagation vector. We contend that this is the helical ferrimagnetism model proposed in previous works,^{16,17} and note that this is precisely in line with the predictions of Mandal *et al.*²⁰

Future work would consist of single-crystal diffraction studies on cryptomelane. Below T_1 , the incommensurate structural modulation would be investigated to determine its propagation vector and structural origin. Single-crystal neutron diffraction would be used to identify the nature of the magnetic ordering below $T_3 \approx 24$ K, and to attempt to distinguish between helical, sinusoidal, and conical magnetic modulations for the incommensurate component of the magnetic structure for $T_3 < T < T_2$. Additionally, neutron studies for a range

of K^+ stoichiometries would be needed to determine the compositional dependence of the magnetic structure.

Funding

LNC and NDK acknowledge a scholarship EP/R513180/1 to pursue doctoral research from the UK Engineering and Physical Sciences Research Council (EPSRC). KS acknowledges funding from the British Council's Newton-Bhabha Fund PhD Placements Programme, which enabled him to visit the University of Cambridge on a research placement. JDB acknowledges support from the Faraday Institution (FIRG016). PB is grateful to Alexander von Humboldt Foundation (Bonn, Germany) for a 2022 Humboldt fellowship for experienced researchers. SED acknowledges funding from EPSRC (EP/T0285580/1).

Acknowledgments

Magnetic and heat capacity measurements at the University of Cambridge were made on the EPSRC Advanced Characterization Suite (funded under EP/M0005/24/1). We acknowledge Diamond Light Source for time on the I11 instrument under BAG proposal CY28349 (December 2021) and rapid access proposal CY33664-1 (October 2022). We acknowledge the Institut Laue-Langevin (ILL) for neutron diffraction measurements on the high-intensity powder diffractometer D20 and the high-resolution powder diffractometer D2B under proposal EASY-893.

LNC thanks Dr Saptarshi Mandal and Dr Efrain E. Rodriguez for useful correspondence.

Data availability

The variable-temperature neutron diffraction data from the ILL is available at doi:10.5291/ILL-DATA.EASY-893.¹⁰¹ The remaining data is available in the University of Cambridge repos-

itory at doi:[XXXXXXXXXXXXXXXXXXXXXXXXXXXX].

Supplementary Information

A document containing Supplementary Information to this article is available.

References

- (1) Byström, A.; Byström, A. M. The crystal structure of hollandite, the related manganese oxide minerals, and α -MnO₂. *Acta Crystallographica* **1950**, *3*, 146–154.
- (2) Liu, X.; Xie, Y.; Hu, Z.; Lin, H.-J.; Chen, C.-T.; Dong, L.; Wang, Q.; Luo, S.-H.; others Tuning the structural stability and spin-glass behavior in the α -MnO₂ nanotubes by Sn ions doping. *Phys. Chem. Chem. Phys.* **2022**, *24*, 12300–12310.
- (3) Richmond, W. E.; Fleischer, M. Cryptomelane, a new name for the commonest of the “psilomelane” minerals. *American Mineralogist: Journal of Earth and Planetary Materials* **1942**, *27*, 607–610.
- (4) Lan, C.; Gong, J.; Liu, S.; Yang, S. Synthesis and magnetic properties of single-crystalline Na_{2-x}Mn₈O₁₆ nanorods. *Nanoscale Research Letters* **2011**, *6*, 133.
- (5) Poyraz, A. S.; Huang, J.; Pelliccione, C. J.; Tong, X.; Cheng, S.; Wu, L.; Zhu, Y.; Marschilok, A. C.; Takeuchi, K. J.; Takeuchi, E. S. Synthesis of cryptomelane type α -MnO₂(K_xMn₈O₁₆) cathode materials with tunable K⁺ content: the role of tunnel cation concentration on electrochemistry. *Journal of Materials Chemistry A* **2017**, *5*, 16914–16928.
- (6) Chong, S.; Wu, Y.; Liu, C.; Chen, Y.; Guo, S.; Liu, Y.; Cao, G. Cryptomelane-type MnO₂/carbon nanotube hybrids as bifunctional electrode material for high capacity potassium-ion full batteries. *Nano Energy* **2018**, *54*, 106–115.

- (7) Sada, K.; Senthilkumar, B.; Barpanda, P. Cryptomelane $K_{1.33}Mn_8O_{16}$ as a cathode for rechargeable aqueous zinc-ion batteries. *Journal of Materials Chemistry A* **2019**, *7*, 23981–23988.
- (8) Antoni, H.; Morales, D. M.; Bitzer, J.; Fu, Q.; Chen, Y.-T.; Masa, J.; Kleist, W.; Schuhmann, W.; Muhler, M. Enhancing the water splitting performance of cryptomelane-type α -(K)MnO₂. *Journal of Catalysis* **2019**, *374*, 335–344.
- (9) Luo, J.; Zhang, Q.; Garcia-Martinez, J.; Suib, S. L. Adsorptive and acidic properties, reversible lattice oxygen evolution, and catalytic mechanism of cryptomelane-type manganese oxides as oxidation catalysts. *Journal of the American Chemical Society* **2008**, *130*, 3198–3207.
- (10) Santos, V. P.; Bastos, S. S. T.; Pereira, M. F. R.; Órfão, J. J. M.; Figueiredo, J. L. Stability of a cryptomelane catalyst in the oxidation of toluene. *Catalysis Today* **2010**, *154*, 308–311.
- (11) Santos, V. P.; Pereira, M. F. R.; Órfão, J. J. M.; Figueiredo, J. L. Mixture effects during the oxidation of toluene, ethyl acetate and ethanol over a cryptomelane catalyst. *Journal of Hazardous Materials* **2011**, *185*, 1236–1240.
- (12) Davó-Quiñonero, A.; Navlani-García, M.; Lozano-Castello, D.; Bueno-López, A. CuO/cryptomelane catalyst for preferential oxidation of CO in the presence of H₂: deactivation and regeneration. *Catalysis Science & Technology* **2016**, *6*, 5684–5692.
- (13) Crespo, Y.; Andreev, A.; Seriani, N. Competing antiferromagnetic and spin-glass phases in a hollandite structure. *Physical Review B* **2013**, *88*, 014202.
- (14) Strobel, P.; Vicat, J.; Qui, D. T. Thermal and physical properties of hollandite-type $K_{1.3}Mn_8O_{16}$ and $(K, H_3O)_xMn_8O_{16}$. *Journal of Solid State Chemistry* **1984**, *55*, 67–73.

- (15) Suib, S. L.; Iton, L. E. Magnetic studies of manganese oxide octahedral molecular sieves: a new class of spin glasses. *Chemistry of Materials* **1994**, *6*, 429–433.
- (16) Sato, H.; Yamaura, J.-I.; Enoki, T.; Yamamoto, N. Magnetism and electron transport phenomena of manganese oxide ion exchanger with tunnel structure. *Journal of Alloys and Compounds* **1997**, *262*, 443–449.
- (17) Sato, H.; Enoki, T.; Yamaura, J.-I.; Yamamoto, N. Charge localization and successive magnetic phase transitions of mixed-valence manganese oxides $K_{1.5}(H_3O)_xMn_8O_{16}$ ($0 < x < 0.5$). *Physical Review B* **1999**, *59*, 12836.
- (18) Luo, J.; Zhu, H.; Zhang, F.; Liang, J.; Rao, G.; Li, J.; Du, Z. Spin-glass like behavior of K^+ -containing α - MnO_2 nanotubes. *Journal of Applied Physics* **2009**, *105*, 093925.
- (19) Luo, J.; Zhu, H.; Liang, J.; Rao, G.; Li, J.; Du, Z. Tuning magnetic properties of α - MnO_2 nanotubes by K^+ doping. *The Journal of Physical Chemistry C* **2010**, *114*, 8782–8786.
- (20) Mandal, S.; Andreev, A.; Crespo, Y.; Seriani, N. Incommensurate helical spin ground states on the hollandite lattice. *Physical Review B* **2014**, *90*, 104420.
- (21) Tseng, L.-T.; Lu, Y.; Fan, H. M.; Wang, Y.; Luo, X.; Liu, T.; Munroe, P.; Li, S.; Yi, J. Magnetic properties in α - MnO_2 doped with alkaline elements. *Scientific Reports* **2015**, *5*, 9094.
- (22) Barudžija, T.; Kusigerski, V.; Cvjetičanin, N.; Šorgić, S.; Perović, M.; Mitrić, M. Structural and magnetic properties of hydrothermally synthesized β - MnO_2 and α - K_xMnO_2 nanorods. *Journal of Alloys and Compounds* **2016**, *665*, 261–270.
- (23) Barudžija, T.; Perović, M.; Bošković, M.; Cvjetičanin, N.; Gyergyek, S.; Mitrić, M. Magnetic memory effect in hollandite-type α - K_xMnO_2 monocrystalline nanorods. *Journal of Alloys and Compounds* **2020**, *820*, 153406.

- (24) Larson, A. M. Frustrated Magnetism and Electronic Properties of Hollandite Oxide Materials (Chapter 4). Ph.D. thesis, University of Maryland, 2017.
- (25) Larson, A. M.; Moetakef, P.; Gaskell, K.; Brown, C. M.; King, G.; Rodriguez, E. E. Inducing ferrimagnetism in insulating hollandite $\text{Ba}_{1.2}\text{Mn}_8\text{O}_{16}$. *Chemistry of Materials* **2015**, *27*, 515–525.
- (26) Melot, B. C.; Tackett, R.; O’Brien, J.; Hector, A. L.; Lawes, G.; Seshadri, R.; Ramirez, A. P. Large low-temperature specific heat in pyrochlore $\text{Bi}_2\text{Ti}_2\text{O}_7$. *Physical Review B* **2009**, *79*, 224111.
- (27) Mukherjee, P.; Dutton, S. E. Enhanced magnetocaloric effect from Cr substitution in Ising lanthanide gallium garnets $\text{Ln}_3\text{CrGa}_4\text{O}_{12}$ (Ln= Tb, Dy, Ho). *Advanced Functional Materials* **2017**, *27*, 1701950.
- (28) Kelly, N. D.; Liu, C.; Dutton, S. E. Structure and magnetism of a new hexagonal polymorph of $\text{Ba}_3\text{Tb}(\text{BO}_3)_3$ with a quasi-2D triangular lattice. *Journal of Solid State Chemistry* **2020**, *292*, 121640.
- (29) Kelly, N. D.; Yuan, L.; Pearson, R. L.; Suard, E.; Puente Orench, I.; Dutton, S. E. Magnetism on the stretched diamond lattice in lanthanide orthotantalates. *Physical Review Materials* **2022**, *6*, 044410.
- (30) Koskelo, E. C.; Liu, C.; Mukherjee, P.; Kelly, N. D.; Dutton, S. E. Free-Spin Dominated Magnetocaloric Effect in Dense Gd^{3+} Double Perovskites. *Chemistry of Materials* **2022**, *34*, 3440–3450.
- (31) Smith, D. R.; Fickett, F. R. Low-temperature properties of silver. *Journal of Research of the National Institute of Standards and Technology* **1995**, *100*, 119–171.
- (32) Debye, P. Zur theorie der spezifischen wärmen. *Annalen der Physik* **1912**, *344*, 789–839.

- (33) Virtanen, P. et al. SciPy 1.0: Fundamental Algorithms for Scientific Computing in Python. *Nature Methods* **2020**, *17*, 261–272.
- (34) Thompson, S. P.; Parker, J. E.; Potter, J.; Hill, T. P.; Birt, A.; Cobb, T. M.; Yuan, F.; Tang, C. C. Beamline I11 at Diamond: A new instrument for high resolution powder diffraction. *Review of Scientific Instruments* **2009**, *80*, 075107.
- (35) Thompson, S. P.; Parker, J. E.; Marchal, J.; Potter, J.; Birt, A.; Yuan, F.; Fearn, R. D.; Lennie, A. R.; Street, S. R.; Tang, C. C. Fast X-ray powder diffraction on I11 at Diamond. *Journal of Synchrotron Radiation* **2011**, *18*, 637–648.
- (36) Coelho, A. A. TOPAS and TOPAS-Academic: an optimization program integrating computer algebra and crystallographic objects written in C++. *Journal of Applied Crystallography* **2018**, *51*, 210–218.
- (37) Rietveld, H. A profile refinement method for nuclear and magnetic structures. *Journal of Applied Crystallography* **1969**, *2*, 65–71.
- (38) Thompson, P.; Cox, D. E.; Hastings, J. B. Rietveld refinement of Debye-Scherrer synchrotron X-ray data from Al_2O_3 . *Journal of Applied Crystallography* **1987**, *20*, 79–83.
- (39) Stephens, P. W. Phenomenological model of anisotropic peak broadening in powder diffraction. *Journal of Applied Crystallography* **1999**, *32*, 281–289.
- (40) Peterse, W. J.; Palm, J. H. The anisotropic temperature factor of atoms in special positions. *Acta Crystallographica* **1966**, *20*, 147–150.
- (41) Rodríguez-Carvajal, J. FullProf. *CEA/Saclay, France* **2001**,
- (42) Richard, D.; Ferrand, M.; Kearley, G. J. Analysis and visualisation of neutron-scattering data. *Journal of Neutron Research* **1996**, *4*, 33–39.

- (43) Le Bail, A.; Duroy, H.; Fourquet, J. L. Ab-initio structure determination of LiSbWO_6 by X-ray powder diffraction. *Materials Research Bulletin* **1988**, *23*, 447–452.
- (44) Rodríguez-Carvajal, J. A program for calculating irreducible representation of little groups and basis functions of polar and axial vector properties. *Program included FullProf Suite, version July-2010, ILL* **2010**,
- (45) Ritter, C. Neutrons not entitled to retire at the age of 60: More than ever needed to reveal magnetic structures. *Solid State Phenomena* **2011**, *170*, 263–269.
- (46) Dollase, W. A. Correction of intensities for preferred orientation in powder diffraction: application of the March model. *Journal of Applied Crystallography* **1986**, *19*, 267–272.
- (47) Vicat, J.; Fanchon, E.; Strobel, P.; Tran Qui, D. The structure of $\text{K}_{1.33}\text{Mn}_8\text{O}_{16}$ and cation ordering in hollandite-type structures. *Acta Crystallographica Section B: Structural Science* **1986**, *42*, 162–167.
- (48) Bocarsly, J. D.; Heikes, C.; Brown, C. M.; Wilson, S. D.; Seshadri, R. Deciphering structural and magnetic disorder in the chiral skyrmion host materials $\text{Co}_x\text{Zn}_y\text{Mn}_z$ ($x + y + z = 20$). *Physical Review Materials* **2019**, *3*, 014402.
- (49) Przeniosło, R.; Sosnowska, I.; Hohlwein, D.; Hauß, T.; Troyanchuk, I. O. Magnetic ordering in the manganese perovskite $\text{CaMn}_7\text{O}_{12}$. *Solid state communications* **1999**, *111*, 687–692.
- (50) Muñoz, A.; Martínez-Lope, M.; Retuerto, M.; Falcón, H.; Alonso, J. Ferromagnetic behavior in $\text{La}(\text{Cu}_{3-x}\text{Mn}_x)\text{Mn}_4\text{O}_{12}$ ($x = 1, 2$) perovskites. *Journal of Applied Physics* **2008**, *104*, 083911.
- (51) Brady, A. B.; Huang, J.; Durham, J. L.; Smith, P. F.; Bai, J.; Takeuchi, E. S.;

- Marschilok, A. C.; Takeuchi, K. J. The Effect of Silver Ion Occupancy on Hollandite Lattice Structure. *MRS Advances* **2018**, *3*, 547–552.
- (52) Boschetti, A.; Gregorkiewitz, M. Cryptomelane nanocrystals: Pseudosymmetry causes anisotropic peak broadening in Rietveld refinement. *Journal of Solid State Chemistry* **2023**, *327*, 124212.
- (53) Brown, I. D.; Altermatt, D. Bond-valence parameters obtained from a systematic analysis of the inorganic crystal structure database. *Acta Crystallographica Section B: Structural Science* **1985**, *41*, 244–247.
- (54) Van Vleck, J. H. The Jahn-Teller Effect and Crystalline Stark Splitting for Clusters of the Form XY_6 . *The Journal of Chemical Physics* **1939**, *7*, 72–84.
- (55) Nagle-Cocco, L. A. V.; Dutton, S. E. Van Vleck Analysis of Angularly Distorted Octahedra using VanVleckCalculator. *Journal of Applied Crystallography* **2024**, *57(1)*, 20–33.
- (56) Rodriguez-Carvajal, J.; Hennion, M.; Moussa, F.; Moudeden, A. H.; Pinsard, L.; Revcolevschi, A. Neutron-diffraction study of the Jahn-Teller transition in stoichiometric LaMnO_3 . *Physical Review B* **1998**, *57*, R3189.
- (57) Baur, W. H. The geometry of polyhedral distortions. Predictive relationships for the phosphate group. *Acta Crystallographica Section B: Structural Crystallography and Crystal Chemistry* **1974**, *30*, 1195–1215.
- (58) Lawler, K. V.; Smith, D.; Evans, S. R.; Dos Santos, A. M.; Molaison, J. J.; Bos, J.-W. G.; Mutka, H.; Henry, P. F.; Argyriou, D. N.; Salamat, A.; others Decoupling Lattice and Magnetic Instabilities in Frustrated CuMnO_2 . *Inorganic Chemistry* **2021**, *60*, 6004–6015.

- (59) Kimber, S. A. J. Charge and orbital order in frustrated $\text{Pb}_3\text{Mn}_7\text{O}_{15}$. *Journal of Physics: Condensed Matter* **2012**, *24*, 186002.
- (60) Nagle-Cocco, L. A. V.; Bull, C. L.; Ridley, C. J.; Dutton, S. E. Pressure Tuning the Jahn-Teller Transition Temperature in NaNiO_2 . *ACS Inorganic Chemistry* **2022**, *61*, 4312–4321.
- (61) Genreith-Schriever, A. R.; Alexiu, A.; Phillips, G. S.; Coates, C. S.; Nagle-Cocco, L. A. V.; Bocarsly, J. D.; Sayed, F. N.; Dutton, S. E.; Grey, C. P. Jahn–Teller distortions and phase transitions in LiNiO_2 : Insights from *ab initio* molecular dynamics and variable-temperature X-ray diffraction. *Chemistry of Materials* **2024**, *36*, 2289–2303.
- (62) Falqueto, J. B.; Clark, A. H.; Kondracki, Ł.; Bocchi, N.; El Kazzi, M. Unveiling the (de-) lithiation mechanism of nano-sized LiMn_2O_4 allows the design of a cycling protocol for achieving long-term cycling stability. *Journal of Materials Chemistry A* **2023**, *11*, 24800–24811.
- (63) Boucher, B.; Buhl, R.; Perrin, M. Magnetic structure of Mn_3O_4 by neutron diffraction. *Journal of Applied Physics* **1971**, *42*, 1615–1617.
- (64) Boucher, B.; Buhl, R.; Perrin, M. Propriétés et structure magnétique de Mn_3O_4 . *Journal of Physics and Chemistry of Solids* **1971**, *32*, 2429–2437.
- (65) Jensen, G. B.; Nielsen, O. V. The magnetic structure of Mn_3O_4 Hausmannite between 4.7 K and Neel point, 41 K. *Journal of Physics C: Solid State Physics* **1974**, *7*, 409–424.
- (66) Kemei, M. C.; Harada, J. K.; Seshadri, R.; Suchomel, M. R. Structural change and phase coexistence upon magnetic ordering in the magnetodielectric spinel Mn_3O_4 . *Physical Review B* **2014**, *90*, 064418.
- (67) Mugiraneza, S.; Hallas, A. M. Tutorial: a beginner’s guide to interpreting magnetic susceptibility data with the Curie-Weiss law. *Communications Physics* **2022**, *5*, 95.

- (68) Regulski, M.; Przeniosło, R.; Sosnowska, I.; Hohlwein, D.; Schneider, R. Neutron diffraction study of the magnetic structure of α - Mn_2O_3 . *Journal of Alloys and Compounds* **2004**, *362*, 236–240.
- (69) Cockayne, E.; Levin, I.; Wu, H.; Llobet, A. Magnetic structure of bixbyite α - Mn_2O_3 : A combined DFT+U and neutron diffraction study. *Physical Review B—Condensed Matter and Materials Physics* **2013**, *87*, 184413.
- (70) Yamamoto, N.; Endo, T.; Shimada, M.; Takada, T. Single crystal growth of α - MnO_2 . *Japanese Journal of Applied Physics* **1974**, *13*, 723.
- (71) Ivanov, S. A.; Tellgren, R.; Ritter, C.; Nordblad, P.; Mathieu, R.; André, G.; Golubko, N. V.; Politova, E. D.; Weil, M. Temperature-dependent multi-k magnetic structure in multiferroic Co_3TeO_6 . *Materials Research Bulletin* **2012**, *47*, 63–72.
- (72) Cooley, J. A.; Bocarsly, J. D.; Schueller, E. C.; Levin, E. E.; Rodriguez, E. E.; Huq, A.; Lapidus, S. H.; Wilson, S. D.; Seshadri, R. Evolution of noncollinear magnetism in magnetocaloric MnPtGa . *Physical Review Materials* **2020**, *4*, 044405.
- (73) Kim, M.; Chen, X. M.; Wang, X.; Nelson, C. S.; Budakian, R.; Abbamonte, P.; Cooper, S. L. Pressure and field tuning the magnetostructural phases of Mn_3O_4 : Raman scattering and x-ray diffraction studies. *Physical Review B* **2011**, *84*, 174424.
- (74) Chung, J.-H.; Hwan Lee, K.; Song, Y.-S.; Suzuki, T.; Katsufuji, T. Low temperature structural instability of tetragonal spinel Mn_3O_4 . *Journal of the Physical Society of Japan* **2013**, *82*, 034707.
- (75) Shannon, R. D.; Prewitt, C. T. Revised values of effective ionic radii. *Acta Crystallographica Section B: Structural Crystallography and Crystal Chemistry* **1970**, *26*, 1046–1048.

- (76) Goodenough, J. B. Theory of the role of covalence in the perovskite-type manganites [La, M(II)]MnO₃. *Physical Review* **1955**, *100*, 564.
- (77) Goodenough, J. B. An interpretation of the magnetic properties of the perovskite-type mixed crystals La_{1-x}Sr_xCoO_{3-λ}. *Journal of Physics and Chemistry of Solids* **1958**, *6*, 287–297.
- (78) Kanamori, J. Superexchange interaction and symmetry properties of electron orbitals. *Journal of Physics and Chemistry of Solids* **1959**, *10*, 87–98.
- (79) Dutton, S. E.; Broholm, C. L.; Cava, R. J. Divergent effects of static disorder and hole doping in geometrically frustrated β-CaCr₂O₄. *Journal of Solid State Chemistry* **2010**, *183*, 1798–1804.
- (80) Regulski, M.; Przeniosło, R.; Sosnowska, I.; Hoffmann, J.-U. Short and long range magnetic ordering in β-MnO₂—a temperature study—. *Journal of the Physical Society of Japan* **2004**, *73*, 3444–3447.
- (81) Cannella, V.; Mydosh, J. A. Magnetic ordering in gold-iron alloys. *Physical Review B* **1972**, *6*, 4220.
- (82) Mulder, C. A. M.; Van Duynveldt, A. J.; Mydosh, J. A. Susceptibility of the Cu Mn spin-glass: Frequency and field dependences. *Physical Review B* **1981**, *23*, 1384.
- (83) Binder, K.; Young, A. P. Spin glasses: Experimental facts, theoretical concepts, and open questions. *Reviews of Modern Physics* **1986**, *58*, 801–976.
- (84) Shirakami, T.; Takematsu, M.; Hirano, A.; Kanno, R.; Yamaura, K.; Takano, M.; Atake, T. Spin glass-like magnetic properties of LiNiO₂. *Materials Science and Engineering: B* **1998**, *54*, 70–72.
- (85) Khan, S.; Aw, E. S. Y.; Nagle-Cocco, L. A. V.; Sud, A.; Ghosh, S.; Subhan, M. K. B.; Xue, Z.; Freeman, C.; Sagkovits, D.; Gutiérrez-Llorente, A.; others Spin-Glass States

Generated in a van der Waals Magnet by Alkali-Ion Intercalation. *Advanced Materials* **2024**, *36*, 2400270.

- (86) Freedberg, J.; Dahlberg, E. D. A brief review of spin glass magnetometry techniques. *Frontiers in Physics* **2024**, *12*, 1447018.
- (87) Yu, J.; Tang, S.; Wang, L.; Du, Y. Spin-glass-like behavior in hollandite $\text{Ba}_{1+\delta}\text{Mn}_8\text{O}_{16}$ nanoribbons synthesized by molten-salt method. *Chemical Physics Letters* **2010**, *496*, 117–121.
- (88) Bai, X.; Paddison, J. A. M.; Kapit, E.; Koochpayeh, S. M.; Wen, J.-J.; Dutton, S. E.; Savici, A. T.; Kolesnikov, A. I.; Granroth, G. E.; Broholm, C. L.; Chalker, J. T.; Mourigal, M. Magnetic Excitations of the Classical Spin Liquid MgCr_2O_4 . *Physical Review Letters* **2019**, *122*, 097201.
- (89) Nilsen, G. J.; Okamoto, Y.; Masuda, T.; Rodriguez-Carvajal, J.; Mutka, H.; Hansen, T.; Hiroi, Z. Complex magnetostructural order in the frustrated spinel $\text{LiInCr}_4\text{O}_8$. *Physical Review B* **2015**, *91*, 174435.
- (90) Funni, S. D.; Ercius, P.; Calderon, S.; Dickey, E. C. The incommensurate modulation of tetragonal tungsten bronze quantified by high resolution 4D STEM. *Materialia* **2026**, 102651.
- (91) Krayzman, V.; Bosak, A.; Playford, H. Y.; Ravel, B.; Levin, I. Incommensurate modulation and competing ferroelectric/antiferroelectric modes in tetragonal tungsten bronzes. *Chemistry of Materials* **2022**, *34*, 9989–10002.
- (92) Song, J. W.; Gao, Y.; Ou, Y. B.; Luo, X. T.; Chen, X. Y.; Wang, W. Y.; Wang, Y.; Wu, S. Y.; Liu, X. Q.; Zhu, X. L.; others Role of Incommensurate Modulation in $\text{Ba}_4(\text{Sm}_{1-x}\text{La}_x)_2\text{Ti}_4\text{Nb}_6\text{O}_{30}$ Tetragonal Tungsten Bronzes. *Chemistry of Materials* **2024**, *36*, 6720–6730.

- (93) Mao, M. M.; Li, K.; Zhu, X. L.; Chen, X. M. Incommensurate and commensurate modulations of $\text{Ba}_5\text{RTi}_3\text{Nb}_7\text{O}_{30}$ (R= La, Nd) tungsten bronzes and the ferroelectric domain structures. *Journal of Applied Physics* **2015**, *117*.
- (94) Stennett, M. C.; Miles, G. C.; Sharman, J.; Reaney, I. M.; West, A. R. A new family of ferroelectric tetragonal tungsten bronze phases, $\text{Ba}_2\text{MTi}_2\text{X}_3\text{O}_{15}$. *Journal of the European Ceramic Society* **2005**, *25*, 2471–2475.
- (95) Nylund, I.-E.; Zeiger, C. R.; Peng, D.; Vullum, P. E.; Walker, J.; Einarsrud, M.-A.; Grande, T. Centrosymmetric tetragonal tungsten bronzes $\text{A}_4\text{Bi}_2\text{Nb}_{10}\text{O}_{30}$ (A= Na, K, Rb) with a Bi 6s lone pair. *Chemistry of Materials* **2022**, *35*, 17–26.
- (96) Randall, C. A.; Markgraf, S. A.; Bhalla, A. S.; Baba-Kishi, K. Incommensurate structures in highly ordered complex perovskites $\text{Pb}(\text{Co}_{1/2}\text{W}_{1/2})\text{O}_3$ and $\text{Pb}(\text{Sc}_{1/2}\text{Ta}_{1/2})\text{O}_3$. *Physical Review B* **1989**, *40*, 413.
- (97) Abakumov, A. M.; Erni, R.; Tsirlin, A. A.; Rossell, M. D.; Batuk, D.; Nénert, G.; Tendeloo, G. V. Frustrated Octahedral Tilting Distortion in the Incommensurately Modulated $\text{Li}_{3x}\text{Nd}_{2/3-x}\text{TiO}_3$ Perovskites. *Chemistry of Materials* **2013**, *25*, 2670–2683.
- (98) Ma, T.; Fan, Z.; Xu, B.; Kim, T.-H.; Lu, P.; Bellaiche, L.; Kramer, M. J.; Tan, X.; Zhou, L. Uncompensated polarization in incommensurate modulations of perovskite antiferroelectrics. *Physical Review Letters* **2019**, *123*, 217602.
- (99) Tuinstra, F.; Berg, A. J. v. d. Isomorphism among commensurate and incommensurate high-temperature phases of A_2BO_4 compounds. *Phase Transitions: A Multinational Journal* **1983**, *3*, 275–282.
- (100) Plesko, S.; Kind, R.; Arend, H. New structural phase sequence with incommensurate phases in A_2BX_4 halides with $\beta\text{-K}_2\text{SO}_4$ structure. *physica status solidi (a)* **1980**, *61*, 87–94.

- (101) Liam A. V. Nagle-Cocco and E. Suard. Elucidating the origin of the magnetic behaviour of cathode material $K_{1.33}Mn_8O_{16}$. Institut Laue-Langevin. *doi:10.5291/ILL-DATA.EASY-893*. 2021; <https://data.isis.stfc.ac.uk/doi/STUDY/113601628/>.